Study of Plasmonic and Magneto-Optical Properties of Transition Metal Doped Indium Oxide Nanocrystals

by

Yi Tan

A thesis

presented to the University of Waterloo

in fulfillment of the

thesis requirement for the degree of

Master of Science

in

Chemistry

Waterloo, Ontario, Canada, 2019

Author's Declaration

I hereby declare that I am the sole author of this thesis. This is a true copy of the thesis, including any required final revisions, as accepted by my examiners. I understand that my thesis may be made electronically available to the public.

Abstract

Plasmonic nanostructure materials have been widely investigated recently because of their considerable potential for applications in biological and chemical sensors, nano-optical devices and photothermal therapy. Compared to metal nanocrystals (NCs), doped semiconductor NCs with tunable localized surface plasmon resonance (LSPR) from near-infrared (NIR) mid-infrared (MIR) region bring more opportunities to the applications of plasmonics. Magnetoplasmonic nanostructures which could be utilized in multifunctional devices also have attracted attention due to the combination of plasmonic and magnetic properties and the manipulation of light with external magnetic fields.

In this research, indium oxide (In_2O_3) as a typical n-type semiconductor with high mobility and carrier concentration is selected as the host lattice for doping, and molybdenum (Mo) and tungsten (W) which are transition metal elements from the same group as dopants. Colloidal molybdenum-doped indium oxide (IMO) NCs and tungsten-doped indium oxide (IWO) NCs with varying doping concentrations have been successfully synthesized, and their plasmonic and magneto-optical properties have been explored. Similarities and differences between IMO NCs and IWO NCs were discussed. Both IMO and IWO NCs have shown good tunability of plasmon resonance in the MIR range approximately from 0.22 eV to 0.34 eV. 9.2 % IMO NCs show the strongest LSPR at 0.34 eV and the maximum free electron concentration of 1.1×10^{20} cm^{-3}, and 1.5 % IWO NCs exhibit the strongest LSPR at 0.33 eV with the free electron concentration of 0.94×10^{20} cm^{-3}. The magneto-optical properties were studied by magnetic circular dichroism (MCD) spectroscopy. The variable-temperature-variable-field MCD spectra that coincide with the band gap absorption, indicate the excitonic splitting in the NCs. A robust MCD intensity at room

temperature suggests intrinsic plasmon-exciton coupling and carrier polarization induced by plasmon, which might be phonon-mediated. A decrease in MCD signal with temperature and the saturation-like field dependence of MCD intensity for IMO and IWO NCs may related to the different oxidation states of the dopant ions since the reduced 5+ oxidation states can exhibit the Curie-type paramagnetism. IMO and IWO NCs show the coupling between exciton and plasmon in a single-phase which opens a possibility for their application in electronics and photonics. Moreover, magnetoplasmonic modes provide a new degree of freedom for controlling carrier polarization at room temperature in practical photonic, optoelectronic and quantum-information processing devices.

Acknowledgement

First, I would like to thank my supervisor Dr. Pavle Radovanovic for his support and guidance during the project. His enthusiasm towards science and curiosity about exploration have inspired me to face and overcome the challenges I met throughout the research. No improvement can be made without trying, failing and stepping out of your comfort zone. It is important for not only becoming a better researcher but also a better person in the whole life. I would also like to express my appreciation to my committee members Dr. Holger Kleinke and Dr. Vivek Maheshwari for their assistance and encouragement during my graduate study.

I would like to express my sincere gratitude to Dr. Howard Siu for his assistance and useful suggestions about writing the thesis. I would also like to acknowledge Dr. Carmen Andrei at McMaster University for her assistance in TEM image collection. I would like to thank Kleinke and Nazar's group at the University of Waterloo, for their guidance and assistance for XRD collection and FTIR measurement.

I would like to thank all my past and current group members, Manu, Vahid, Paul, Natalie, Terry, Hanbing, Susi, Enas, Yunyan, Shuoyuan, Nathaniel, and Luna for their advice and assistance. Specifically, I would like to thank Terry for always being willing to help and gave me a lot of good suggestions for my research. I would also like to thank Hanbing who helped me build a good start with my research. In addition, I would like to acknowledge Natalie for the X-ray absorption spectroscopy data analysis which requires much effort and time.

Finally, I would like to thank my family and my friends for their support and encouragement during these years. I could not have come this far without them.

Table of Contents

List of Figures

List of Tables

List of Abbreviations

Acac	Acetylacetonate
a.u.	Atomic Units
bcc	Body-centered Cubic
CB	Conduction Band
FTIR	Fourier Transform Infrared Spectroscopy
HRTEM	High-resolution TEM
LSPR	Localized Surface Plasmon Resonance
IMO	Molybdenum-doped Indium Oxide
IWO	Tungsten-doped Indium Oxide
MCD	Magnetic Circular Dichroism
MIR	Mid-Infrared
NCs	Nanocrystals
rh	Rhombohedral
SPR	Surface Plasmon Resonance
TCOs	Transparent Conducting Oxides
TEM	Transmission Electron Microscopy
UV-Vis-NIR	Ultraviolet-Visible-Near-Infrared Spectroscopy
VB	Valence Band
XAS	X-ray absorption spectroscopy
XPS	X-ray Photoelectron Spectroscopy
XRD	X-ray Diffraction

Chapter 1. Introduction

1.1 Semiconductor Nanocrystals and Transparent Conducting Oxides

A semiconductor is a material with its electrical conductivity between a conductor and an insulator. In various materials electrical conductivities can be different depending on the size of the band gap, the energy difference between the upper edge of the valence band (VB) which is fully filled with electrons, and the lower edge of the conduction band (CB) which is empty. For conductors, the blurred distinction between the VB and CB can result in a very small band gap or no band gap, which allows the electrons to easily move to the higher energy levels.[1] In the case of insulators, the energy difference between VB and CB is large, so the band gap prevents electrons from transferring.[1]

In semiconductors, however, as they have moderate band gaps, electrons can be excited from lower band to the upper band if appropriate energy is applied.[1] A semiconductor that can exhibit semiconducting properties naturally is called intrinsic semiconductor, such as silicon and germanium.[1] Another type of semiconductors that is modified by doping with some other elements with energy levels close to those of the host lattice material are called extrinsic semiconductors. [1,2] When the dopant element with energy levels near the CB has more valence electrons than the host material, and can donate the electrons to the CB, the doped extrinsic semiconductor can be classified as an n-type semiconductor. If the doping material with energy levels close to the VB has fewer electrons than the host and can provide positive holes to accept the electrons from the VB, a p-type semiconductor is formed.[1] Figure 1.1 shows the band structures of intrinsic semiconductor, n-type and p-type semiconductors.

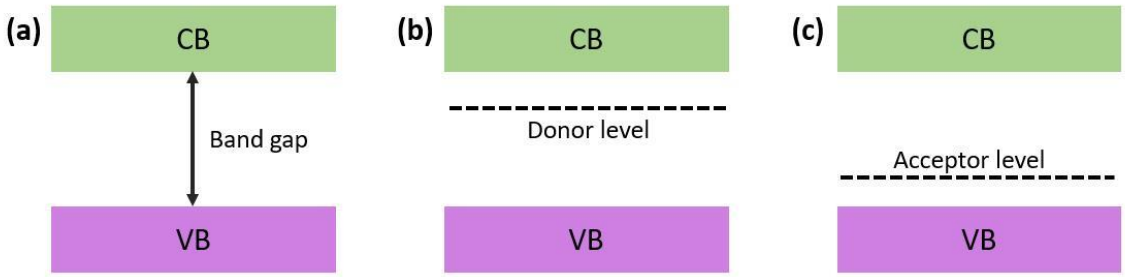

Figure 1.1: Illustration of band structure for (a) intrinsic semiconductor, (b) n-type semiconductor with donor level close to the CB and (c) p-type semiconductor with acceptor level close to the VB.

Semiconductor nanocrystals (NCs) have attracted attention in recent years due to their tremendous potential in a wide range of applications, such as nanoscale electronic devices, chemical sensors, biosensors and solar cells.[2,3] Compared to bulk semiconductors, the physical and chemical properties of semiconductor NCs can be dramatically different and unique because of the large surface area or the quantum confinement effect. By controlling the size and shape of semiconductor NCs, their conductivities and optical properties can be tunable.[2]

Transparent conducting oxides (TCOs) as one important type of semiconductors also have become a hot topic in recent years for their wide applications in many different industrial fields. With high transparency and low resistivity, TCOs play important roles in flat panel displays, transparent electrodes in solar cells, thin film photovoltaics and smart windows.[4–6] Some metal oxides such as indium oxide (In_2O_3), zinc oxide (ZnO), and tin oxide (SnO_2) are nowadays industrially significant TCOs.[4] Improving the mobility and increasing the electrical

conductivity while simultaneously maintaining the high optical transparency have been the main focus in the development of TCOs.[7]

1.2 Indium (III) Oxide and Its Phase Transformation

Indium (III) oxide (In_2O_3), which has been widely exploited in commercial products such as sensors, batteries, displays and electrodes, is a typical n-type TCO semiconductor with a relatively wide band gap around 3.75 eV; it exhibits high mobility as well as high charge carrier concentration and shows no absorption in the visible region from 400 to 800 nm.[8–10] As a polymorphic semiconductor, In_2O_3 has two distinct phases, the stable body-centered cubic bixbyite structure (bcc-In_2O_3) and the metastable rhombohedral corundum structure (rh-In_2O_3).

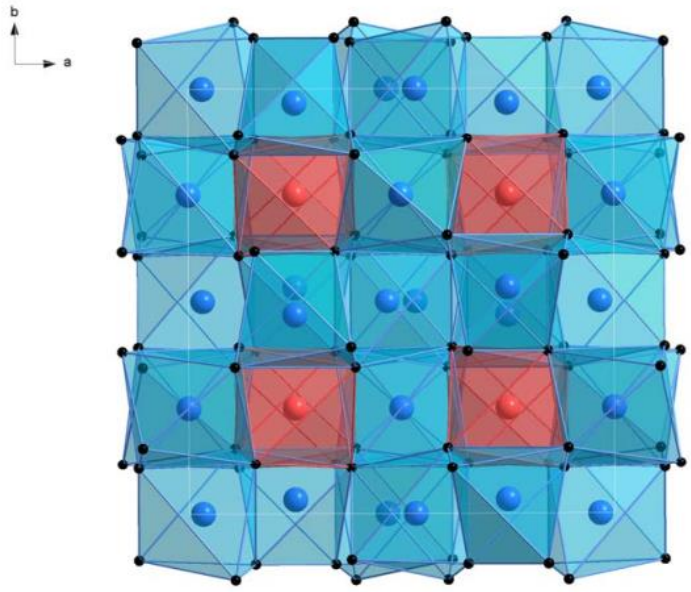

Figure 1.2: Unit cell of cubic bixbyite-type In_2O_3 (bcc-In_2O_3) crystal lattice viewed along c-axis. Indium ions reside in two characteristic sites, known as b and d-sites, which are shown as red and blue spheres, respectively. Oxygen ions are shown as smaller black spheres.[10]

In cubic bixbyite-type In_2O_3 (bcc-In_2O_3), there are two characteristic six-coordinate sites, b- and d-sites, where the In^{3+} cations reside, corresponding to the red and blue spheres shown in Figure 1.2, respectively. One-quarter of indium cations occupy the b-sites which have S_6 point group symmetry, and the remaining three-quarters of indium cations occupy d-sites (point group: C_2) which are highly distorted.[11,12]

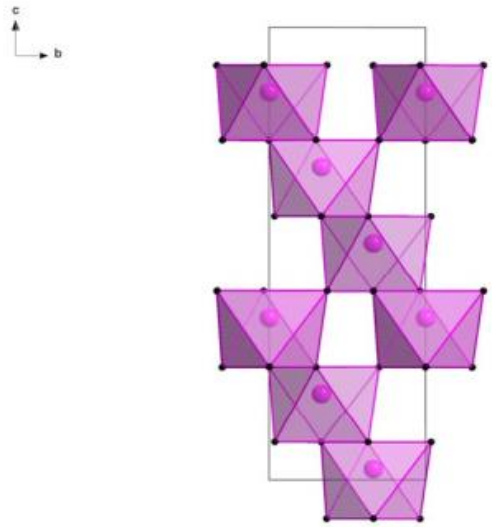

Figure 1.3: Unit cell of rhombohedral corundum-type In_2O_3 (rh-In_2O_3) crystal lattice viewed along a-axis. Indium ions are shown as purple and oxygen ions as black spheres.[10]

The unit cell of metastable rhombohedral corundum-type In_2O_3 (rh-In_2O_3) in Figure 1.3 shows that oxygen anions form a hexagonal close-packed structure and indium cations occupy two-thirds of the six-coordinate sites.[10] Some optical and physical properties of rh-In_2O_3 might be different from bcc-In_2O_3 due to their different crystal structures.[13,14] Although many studies and research interests focus on bcc-In_2O_3 as it is the stable phase, exploring the stabilization of metastable rh-In_2O_3 and the transformation between rh-In_2O_3 and bcc-In_2O_3 could be beneficial in expanding the application of In_2O_3 NCs.

In_2O_3 with the metastable corundum phase can be obtained and stabilized through applying high temperatures and pressures to cubic bixbyite-type In_2O_3.[15,16] In this solid state synthesis, harsh conditions of 65 GPa and 1250 °C are required.[15] Some previous research has also reported that rh-In_2O_3 can be prepared directly through the calcination of indium precursors, such as $In(OH)_3$ and InOOH, under ambient pressure.[17,18] Furthermore, to get a better understanding of the In_2O_3 NCs growth and the phase transformation between rh-In_2O_3 and bcc-In_2O_3, it has been demonstrated that when colloidal In_2O_3 is synthesized in solution, rh-In_2O_3 is actually a transient structure during the formation of bcc-In_2O_3 NCs.[10] The size of the nanocrystals can be a critical factor which directly correlates to the stabilization of the nanocrystal structure.[10,14,19] In this case, 5 nm was found to be the critical size for the phase transformation of In_2O_3 NCs, and both bcc- and rh-In_2O_3 NCs can be obtained in the same reactions through size selective precipitation.[10,20] In_2O_3 NCs with size smaller than 5 nm show a tendency to be stable in the rhombohedral phase, and with the increasing size above 5 nm, bcc-In_2O_3 NCs are observed.[20,21]

According to some studies, particle surfaces have a huge effect on the phase transformation process for NCs with small sizes and the relative stabilities of different phases can be reversed by the surface free-energy contribution.[10,22,23] In other words, high surface area, which is a result of large surface to volume ratios in reduced dimensions, can help stabilize metastable phases because of the increased surface free-energy.[10,23] In addition, the surface local electron density can also influence the stability of different polymorphs.[10,20] Surface interatomic distances increase due to the higher electron density on surfaces, which causes a compressive surface stress to counteract the charge density difference.[20] In_2O_3 in the rhombohedral phase is

more favorable and stable in this case since the rh-In_2O_3 NC has a more close-packed crystal structure as the density of rh-In_2O_3 is higher than bcc-In_2O_3 by *ca.* 2.6%.[16]

Based on the phase transformation study, colloidal In_2O_3 NCs with specific phase and size have been synthesized under different experimental conditions, such as precursors, solvent and temperature.[22] In order to manipulate the optical and electronic properties of In_2O_3 and related materials, the control of phase structure can be a crucial issue.

1.3 Aliovalent Doping of Nanocrystals and Doping Mechanism

Dopants, or intentionally incorporated of impurities, have played a critical role in the research of semiconductor nanocrystals. It has been explored that the size, shape, optical behavior as well as electronic properties of semiconductor nanocrystals can be manipulated to some extent through doping.[10,13,24] There is generally a valence state difference between the host atom and the substitutional impurity, which is termed aliovalent doping. For instant, a n-type doping is when the dopant cation has more valence electrons than the host cation and can donate extra electrons while a p-type doping is the opposite that the substitutional atom with fewer valence electrons can provide extra holes to the host lattice.[1,24]

To synthesize a nanocrystal material, the precursors that contain the constituent elements are required. Solid-phase, liquid-phase and gas-phase reactors have been utilized to achieve the synthesis of nanocrystals. In addition, colloidal chemistry is considered to be the approach that can yield the most uniform crystallites.[24] To intentionally introduce impurities into the host lattice, the most common method is to include a precursor that containing the doping atoms in the synthesis and different characterization measurements can be performed to investigate the incorporation of the dopants.[24]

Moreover, different nanocrystal doping models are proposed to explain the mechanism of doping. The Turnbull model states that doping is governed by statistics and the solubility of dopants is the same as in the bulk, therefore, the crystallites are basically pure since they contain few atoms.[24,25] However, this model cannot make an explanation of the fact that some dopants are sufficiently soluble in the bulk but not in the nanocrystals.[24]

An alternative model called self-purification focuses on thermodynamics. It considers that the dopants solubility is much lower in the nanocrystals, which implies that it is difficult for impurities to be doped into nanocrystals.[24,26] Besides, doping atoms can be readily expelled from the nanocrystals to surface due to thermodynamic reasons.[24] As the fundamental assumption of self-purification model is that thermodynamic equilibrium with environment, including chemical equilibrium with dopants and host lattice constituents, is achieved in the nanocrystals, doping atoms need to diffuse facilely through the nanocrystals. Therefore, this model can be applied to the solid- or gas-phase synthesis for which the reaction is allowed to be above 1000 °C, but not suitable for the liquid-phase synthesis which undergoes low temperature and cannot realize the rapid diffusion of dopants.[24,26]

The trapped dopant model is established for most liquid-phase synthesis where the kinetic factors is dominated in the doping process.[24] In this case, adsorption of impurity atoms occurs on the surface of the nanocrystals and then dopants are further trapped within the growth of the material.[27] The structure and shape of nanocrystals play important roles in this doping mechanism since they can influence the surface properties which are critical for dopant binding.[24] In addition, appropriate surfactants should be chosen in the colloidal synthesis to make sure the binding between surfactants and NC surface or impurity is moderate.[24]

In the past few years, different dopants have been explored in the incorporation of colloidal In_2O_3 NCs. For example, chromium-doped In_2O_3 (Cr: In_2O_3), europium-doped In_2O_3 (Eu: In_2O_3), tin-doped In_2O_3 (Sn: In_2O_3), antimony-In_2O_3 (Sb: In_2O_3), and titanium-doped In_2O_3 (Ti: In_2O_3) NCs have been successfully synthesized and well characterized.[13,20,28–30] Among these nanocrystals, one of the most important properties, which is also the focus of this research, that has been introduced into the doped In_2O_3 host lattice through doping is called localized surface plasmon resonance.

1.4 Localized Surface Plasmon Resonance

Materials with plasmonic properties have become a hot research topic in recent years due to their considerable potential for applications in biological and chemical sensors, photothermal cancer therapy, nano-optical devices and molecule-specific imaging.[31–36] In physics, a plasmon is defined as a quantum of plasma oscillation and can be used to describe a collective oscillation of free electrons.[37] Surface plasmon resonance (SPR), as a form of plasmon that occurs at the surface of a material, is the resonant oscillation of surface electrons stimulated by incident light.[38] When SPR is confined in a nanosized material which is smaller or comparable to the wavelength of incident light, it is known as localized surface plasmon resonance (LSPR).[37] In addition, for LSPR, oscillations near the surface of the nanoparticle can be enhanced dramatically but also drop off quickly with increasing distance away from the surface.[37] The illustration of LSPR is shown in Figure 1.4.

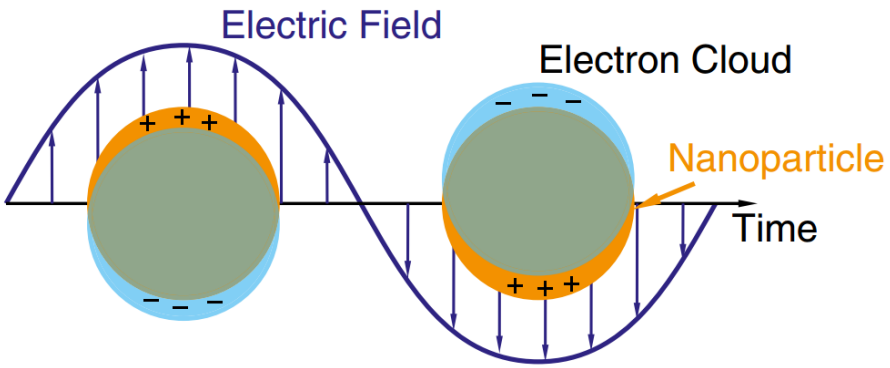

Figure 1.4: Schematic of localized surface plasmon resonance (LSPR). The oscillating electric field of the incident light can induce coherent oscillations in the free electrons of the nanoparticles.[39]

Localized surface plasmon resonance was considered to exist only in traditional noble metal nanostructures in the past. Two typical examples are gold and silver nanoparticles, which can exhibit LSPR absorption in the visible region with large charge carrier concentrations ($\sim 10^{23}$ cm^{-3}) .[36,40]

However, with the study in the semiconductor nanocrystals, LSPR generally can be seen as the optical signatures of charge carriers.[36] It has been demonstrated that doped TCO semiconductor nanostructures can exhibit LSPR as well as metallic nanocrystals. The plasmon resonance frequencies of these doped semiconductor nanocrystals commonly appear in the NIR and MIR region because of their low charge carrier densities compared to those of noble metals.[36] Through different types of doping, the carrier concentrations in doped TCOs can range from 10^{16} to 10^{21} cm^{-3}.[40]

Research interests in plasmonics has recently focused on tuning the particle size, shape, composition, defect concentration, and medium dependence of nanostructured materials, since

these properties have significant effects on the LSPR frequencies.[40] One typical type of tunability that semiconductors can provide over noble metals is the free carrier concentration. The modified Drude-Lorentz theory, which originated from the free electron gas model for metals, can be used to describe the relationship between the free carrier concentration and the plasmon band quantitatively.[41] The equations are shown below:

$$\alpha_{free\ electrons} = \frac{Ne^2}{m^*\varepsilon_0 nc\tau\omega^2} \qquad \text{eq. 1.1}$$

$$\omega_p = \sqrt{\frac{Ne^2}{m^*\varepsilon_{opt}\varepsilon_0}} \qquad \text{eq. 1.2}$$

where α is the absorption coefficient related to the free electrons, ω_p is the energy position of the plasmon band, N is the charge carrier concentration, e is the electron charge, m^* is the effective mass of an electron, ε_0 is the vacuum permittivity, τ is the mean time between two electron scattering events, n is the refractive index of undoped semiconductor, and c and ω are the speed and frequency of light, respectively; and ε_{opt} is the dielectric constant measured in the transparent region of the spectrum of an undoped semiconductor, which is equal to n^2.

From the equations above, it can be concluded that the absorption coefficient α is directly proportional to the charge carrier concentration N while the energy position of the plasmon band, ω_p, is proportional to the square root of N. Since different doping concentrations result in various charge carrier concentrations, the plasmon resonance frequencies of doped semiconductor NCs can be tuned over a wide range. Conversely, the lack of tunability of free carrier concentration,

low transparency and high losses of LSPR in the near- and mid-infrared region of noble metal nanostructures limit their applications.[42]

1.5 Doped Semiconductor Nanocrystals with Plasmonic Properties

As mentioned above, semiconductor NCs can exhibit plasmonic properties through doping and their LSPR frequencies can be altered by varying the doping concentration. Because of the wide, tunable LSPR absorption range, in addition to low cost and controllable size of doped semiconductor NCs, many different kinds of host lattice materials and dopants have been explored, such as tin-doped indium oxide (Sn: In_2O_3), antimony-doped indium oxide (Sb: In_2O_3), aluminum doped zinc oxide (Al: ZnO), and indium-doped cadmium oxide (In: CdO), *etc*.[20,28,36,43,44]

Previous research has seen successful synthesis of colloidal ITO with a series of concentrations by changing the initial [Sn]/[In] precursor ratios. Only bcc-ITO NCs shown LSPR absorption in the NIR region.[10] Based on the study by Kanehara *et al.*, it has been demonstrated that by changing the concentration of Sn doping from 3 to 30 mol %, the LSPR absorption peaks of ITO NCs can be readily tuned from 1618 to greater than 2200 nm.[36] Their results also indicated that 10% Sn doped In_2O_3 gives the highest electron carrier concentration in the ITO NCs, as the maximum of the LSPR absorption is located at the shortest wavelength of 1618 nm.[36]

Furthermore, differing from noble metal nanostructures, ITO shows no inter- and intraband transitions in the visible-near-infrared (Vis-NIR) region, which gives it high optical transparency in the visible region.[36] Some other advantages of ITO and other doped semiconductor NCs are their low costs, controllable NC sizes and chemical stabilities compared to noble metal NCs. Due to these advantages as well as the controllable LSPR absorption

frequencies in the NIR to MIR region, doped semiconductor nanocrystals with plasmonic properties expand the potential applications of plasmonics, such as thermal imaging, chemical sensing and surface-enhanced infrared absorption spectroscopy.[36,45]

Doping semiconductors also leads to the change of the electronic structure. For n-type semiconductor nanocrystals, the interaction between dopants can result in the emergence of a dopant sub-band near the edge of the conduction band, and tail states arise as well because of the distortions in the crystal structure.[46] The exchange energy with the extra carriers and the modified screening of the valence electron exchange energy can both reduce the energy band gap and result in the band gap narrowing.[47] On the other hand, the absorption measurement of doped n-type semiconductors may show blue shift due to the conduction band states occupied by the extra electrons, which is referred to as the Moss-Burstein effect. Since the optical measurement involves all these effects, the competition between them determine the measured optical band gap.[28,48]

1.6 Plasmon-Exciton Coupling and Magneto-Plasmonics

The collective oscillations of free electrons in plasmonic nanoparticles have been proposed for applications in multifunctional quantum devices. In the study of nanotechnology, one of the representative and fundamental problems is the electronic interactions at the nanoscale.[49] It has been reported that with the utilization of metallic plasmonic nanocrystals, light-electron interactions which are able to tune electromagnetic field distributions and localize light energy can be manipulated via different methods.[50]

Two typical excited states in the nanostructures are plasmons and excitons, and it has been shown that coupled electronic systems can be produced through these two excited states.[49]

Specifically, the excitonic absorption and emission, and the Raman scattering intensities can be enhanced via resonant coupling between a plasmon and an exciton.[51,52] Therefore, one interesting phenomenon that has particularly attracted many attentions is the plasmon-exciton interaction observed in heterostructure nanomaterials. For instance, it has been demonstrated that large photoluminescence enhancement of visible emission from InGaN/GaN quantum well materials coated with Ag thin films was achieved because of the exciton-surface-plasmon coupling.[51,53] Based on their experimental results, high-efficiency light-emitting diodes (LEDs) could be one important potential future application of plasmonics considering the increasing demand of illumination.[53]

Moreover, according to Kotov et al., the exciton-plasmon interactions are confirmed in the semiconductor-metal nanocomposites.[49] The CdTe nanowires, which have mobile excitons and the Au nanoparticles, which can produce localized plasmons, are connected by "molecular springs", and the distance between the plasmon and the exciton can be reversibly altered.[49] The wavelength shift of the nanocomposites depends on the exciton-plasmon interactions, which are related to the distance between the nanowire and the nanoparticle.[49] Similar plasmon-exciton resonant coupling has been observed in the colloidal metal-semiconductor core-shell nanostructure as well.[54] In their designed Au-CdSe hetero-nanostructures, optical Stark effect as well as the spin manipulation can be enhanced and tailored with the tuning of plasmon resonance.[54]

Spintronics, or spin electronics, as an emerging electronic technology, involves the use of the electron spin as an additional degree of freedom.[55] By using the spin degree of freedom in conventional semiconductor charge-based electronics, the performance and capability of electronic devices can be significantly improved.[56] The interaction between spin and charge of

the carriers results in the spin-dependent effects which means the carrier spin polarization can be manipulated using magnetic field.[56] Previous research also addresses the possibility of using spintronics in individual semiconductor nanostructures.[57] Compared with conventional semiconductor devices, spintronics can potentially increase data processing speed and decrease electric power consumption.[56]

Magneto-plasmonics has also become one of the emerging research topics since it develops unique possibilities to manipulate light by utilizing external magnetic fields or magnetic materials.[50,58,59] For example, an enhancement of Kerr effect, which refers to the rotation of the polarization of reflected light, has been achieved in a magneto-optical material that combines a smooth film of ferromagnetic iron garnet and a nanostructured layer of gold.[60] Although the enhancement of magneto-optical effects in plasmonic nanostructures, and the influence of magnetic field on the surface plasmon resonance are important topics in magneto-plasmonics, the integration of plasmonics and spintronics still needs to be investigated.[50,56,59] The generation of spin currents through surface plasmon resonance by using gold nanoparticles embedded in $Pt/BiY_2Fe_5O_{12}$ bilayer films has demonstrated the manipulation of the carrier polarization with the help of induced plasmon resonance.[50,52]

Free electrons that generate LSPR experience Lorentz force (**F**) when an external electric and magnetic field is applied.[52] The Drude model can be used to express the force of free electron oscillations as shown below[52]:

$$\mathbf{F} = m\left(\frac{\mathrm{d}\mathbf{v}}{dt}\right) + \gamma m\mathbf{v} = -e\mathbf{E} - e(\mathbf{v} \times \mathbf{B}) \qquad \text{eq. 1.3}$$

where **E** is the external electric field, **B** is the external electric field, *m*, **v** and *e* are the effective mass, velocity and charge of the electron, respectively, and γ is the damping factor.

When free electrons are excited by circularly polarized light and the external magnetic field is zero, two degenerate cyclotron plasmonic modes with the resonance frequency ω_0 are formed.[52] However, when an external magnetic field along the light propagation direction is applied, the two degenerate plasmonic modes split into two different magnetoplasmonic modes with resonance frequencies ω_B^- and ω_B^+ due to the absorption difference of left circularly polarized (LCP (ρ-)) and right circularly polarized (RCP (ρ+)) beams.[52,61]

Therefore, magnetic circular dichroism (MCD) spectroscopy, which can measure the differential absorption between the LCP and RCP light is performed in this research. The basic experimental set-up of MCD spectroscopy is shown in Figure 1.5.

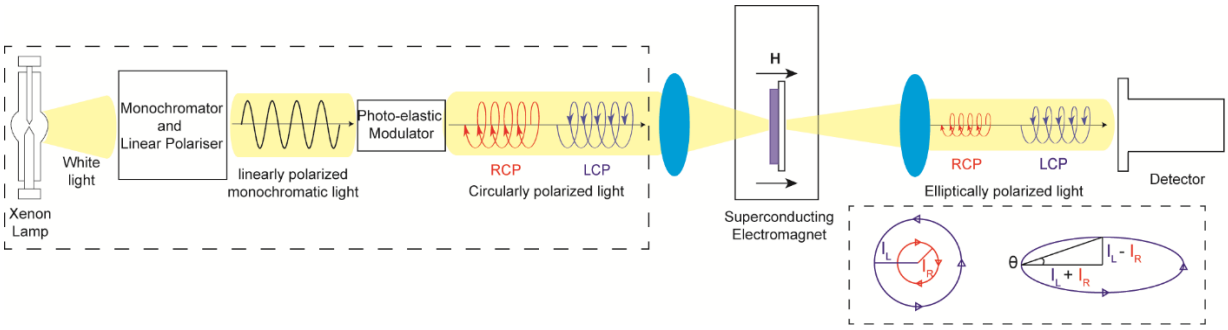

Figure 1.5: Schematic of MCD experimental set-up. [52]

The LCP and RCP light are created when the white light source passes through a monochromator and polarizer and followed by a photo-elastic modulator. After passing through the sample, which is placed in a superconducting magnetooptical cryostat, LCP and RCP light are absorbed and the different intensities, I_L and I_R result in an elliptically polarized beam. The detected ellipticity (θ) can be converted into differential absorption using the eq. 1.4, where $\Delta A = A_L - A_R$, and A_L and A_R are the absorption of LCP and RCP light.

$$\frac{\Delta A}{A} = \frac{\theta}{39326 \times A} \qquad \text{eq. 1.4}$$

The MCD intensity relates to a transition from ground state to an excited can be described as:

$$\frac{\Delta A}{E} = \gamma \mu_B B \left[A_1 \left(-\frac{\partial f(E)}{\partial E} \right) + \left(B_0 + \frac{C_0}{kT} \right) f(E) \right] \qquad \text{eq. 1.5}$$

where $E = h\nu$, γ is the coefficient factor, μ_B is the Bohr magneton, and B is the external magnetic field. A_1, B_0 and C_0 represent the MCD A, B and C terms, respectively. $f(E)$ and $\frac{\partial f(E)}{\partial E}$ are the absorption spectrum band shape and its first derivative. In Figure 1.6, a derivative MCD spectrum of LSPR in plasmonic nanocrystals is generated as an example.

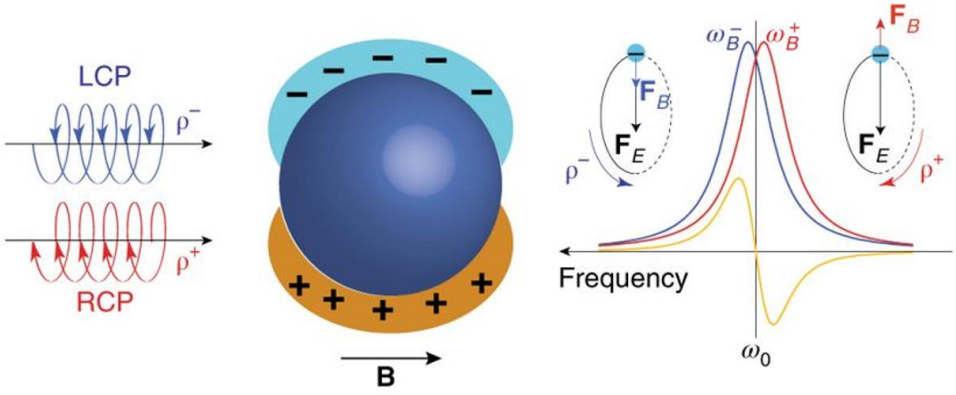

Figure 1.6: Schematic of the origin of MCD spectrum of LSPR in plasmonic nanocrystals. The applied external magnetic field (**B**) is parallel to the light propagation direction. The splitting of the cyclotron plasmonic modes in the magnetic field arises from the different orientation of the magnetic component ($\mathbf{F}_B$) relative to the electric component ($\mathbf{F}_E$) of the Lorentz force.[52]

The LCP (ρ−) beam and RCP (ρ+) beam with the blue and red curved arrows, respectively, showing their cyclotron motion of free electrons are presented on the left. The corresponding magnetoplasmonic modes with resonance frequencies ω_B^- (blue line) and ω_B^+ (red line) are shown on the right, and the yellow line is the MCD spectrum of LSPR in plasmonic

nanocrystals which originates from the absorption difference between the LCP (ρ−) beam and RCP (ρ+) beam.

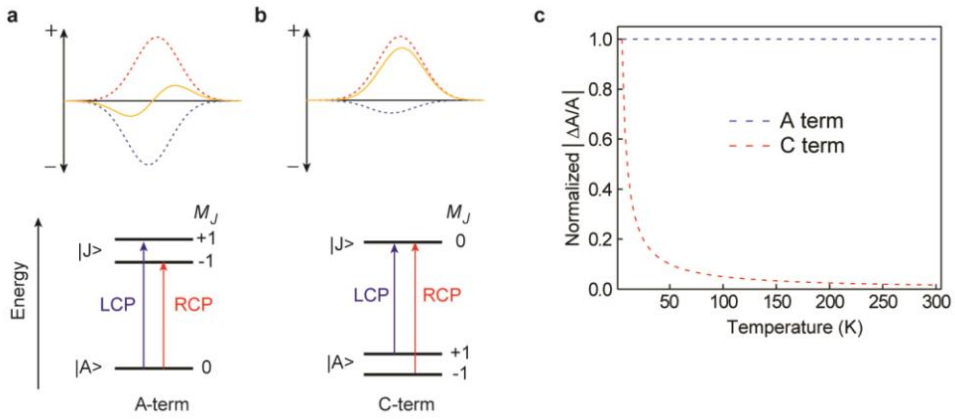

Figure 1.7: Schematic representation of MCD terms. (a) A-term MCD signal (top) and its Zeeman splitting (bottom). (b) C-term MCD signal (top) and its Zeeman splitting (bottom). (c) Comparison of the temperature-dependent A-term and C-term MCD intensity.[52]

Figure 1.7 shows the illustration of A-term and C-term MCD signals. Zeeman splitting are induced because of the external magnetic field. Opposite absorption bands for LCP and RCP light (blue and red lines, respectively) are assigned owing to the small Zeeman splitting. A-term MCD, which is independent with temperature, is associated with the Zeeman splitting of the degenerate excited states. The slight shift in energy results in the MCD signal with derivative shape (yellow line in a). C-term MCD which relates to the Zeeman splitting of the degenerate ground states is different from A-term. As the result of absorption difference in LCP and RCP light, the absorption band shaped MCD signal (yellow line in b) can be observed since there is no splitting of excited state and the low population of the higher energy ground state.[52] Figure 1.7 (c) clearly shows that A-term MCD is independent of temperature while C-term MCD is

temperature dependent and follows Curie-type behaviour. The Curie-type relationship with MCD intensity can be written as:

$$M = \frac{N}{T} \qquad \text{eq. 1.6}$$

where T is the temperature and N is the fitting parameter. The eq. 1.6 was used to fit the temperature dependence of MCD spectra in the following chapters.

It has been shown that MCD spectroscopy can be extremely helpful in the study of the magnetoplasmonic properties.[52,61,62] The linear dependence of the MCD intensity as a function of the magnetic field and the temperature independence of the MCD intensity have been observed for LSPRs in doped semiconductor nanocrystals such as tin-doped indium oxide (ITO) nanocrystals and photodoped colloidal ZnO nanocrystals.[62,63] These two characteristics are also considered to be the signatures of LSPR in plasmonic nanocrystals.[52,62]

1.7 Motivations and Scope of the Thesis

The motivation of this research is to explore new types of semiconductor nanocrystals with tunable LSPR frequencies that can be potentially applied in multifunctional quantum devices. Although there are studies about the plasmon-exciton coupling and magnetoplasmonic properties of nanostructured materials as mentioned above, most of them are based on heterostructures such as core-shell nanocrystals or semiconductor-metal nanocomposites.[50,54,59]

Through the combination of noble metal nanocrystals and paramagnetic or ferromagnetic material, the resonant coupling between exciton transitions and surface plasmon oscillations can be achieved. However, there is still a lack of research of plasmon-exciton coupling in single-

phase semiconductor nanocrystals due to the non-resonant nature of plasmon and exciton and the lack of suitable experimental approach.

Therefore, this study aims to investigate the synthesis of new In_2O_3-based plasmonic NCs interface-free coupling between a plasmon and exciton as well as the control of carrier polarization in doped semiconductor nanocrystals with plasmon resonance. In_2O_3, as a representative n-type TCO semiconductor with high mobility and carrier concentration, is an appropriate host lattice for doping. Two different transition metals Mo and W are used as new dopant elements in In_2O_3 NCs and to induce intense LSPR properties into the host lattice since they have not been explored before in the study of nanocrystals. In addition, physical and optical properties can be systematically correlated in the doped In_2O_3 NCs because Mo and W are transition metals from the same group.

The Mo and W doped In_2O_3 NCs were synthesized by colloidal synthesis method, and the tunability of LSPR frequencies in the MIR region was realized via altering the doping concentrations. MCD spectroscopy was then utilized to explore the interactions between the exciton transitions and the cyclotron magnetoplasmonic modes in the synthesized single-phase plasmonic semiconductor nanocrystals. A non-resonant coupling of the exciton with the magnetoplasmonic modes was discovered.

In the study of these two metal-doped In_2O_3 NCs, various characterization techniques were employed to study the crystal structures, morphology, optical properties as well as the plasmon-exciton coupling of as-synthesized nanocrystals. Results and analysis of the measurements were discussed for both doping systems. Based on the research in this thesis, Mo and W doped In_2O_3 NCs could be new plasmonic nanomaterials that expand the selections of doped semiconductor nanocrystals. Their tunable LSPR in the MIR region potentially enable

new application such as thermal imaging and chemical sensors.[28,37] Moreover, the plasmon–exciton coupling and polarization of carriers investigated by MCD spectroscopy open up the possibility for applications in practical photonic and quantum information processing devices.[52]

Chapter 2. Experimental Methods

2.1 Materials

All reagents and solvents are commercially available and used as provided without any further purification. Indium(III) acetylacetonate ($In(acac)_3$, 98%) and tungsten hexacarbonyl ($W(CO)_6$) were purchased from Strem Chemicals. Bis(acetylacetonato)dioxomolybdenum(VI) ($MoO_2(acac)_2$), oleylamine (70%), and oleic acid (90%) were purchased from Sigma-Aldrich. Toluene (99.9%) and hexane (98.5%) were obtained from Sigma-Aldrich and used as solvents.

2.2 Synthesis Methods

2.2.1 Synthesis of Molybdenum Doped Indium Oxide

The synthetic method for molybdenum-doped indium oxide (IMO) NCs in this research was based on the experimental procedure reported by Wang *et al*..[20] In a 100 mL three-neck round-bottom flask, 0.9 g of $In(acac)_3$, 7.2 g of oleylamine and various amounts of $MoO_2(acac)_2$ were mixed together. The reaction mixture was heated to 250 °C within one hour under the flow of argon and then allowed to react for another one hour with stirring. When the reaction was finished, the mixture was slowly cooled to room temperature and the precipitate was collected by centrifugation. After the precipitate was washed with ethanol three times, 1.5 mL oleic acid was added, and the mixture was heated to 90 °C using an oil bath for 30 minutes. This procedure was done to remove any surface-bound dopant ions and impurities.[29] Subsequently, the sample was precipitated again and washed with ethanol three times. The final product was separated into

two parts. One part was dried and collected as a powder, and the remaining part was dispersed in a non-polar solvent, such as hexane or toluene.

2.2.2 Synthesis of Tungsten Doped Indium Oxide

The synthetic method for tungsten-doped indium oxide (IWO) NCs was similar to the synthesis of IMO NCs shown above with some modifications. Same amount of $In(acac)_3$ and oleylamine, and various amounts of $W(CO)_6$ were mixed together in a 100 mL three-neck round-bottom flask. The reaction mixture was heated to 300 °C within one hour under the flow of argon and allowed to react for another one hour with stirring. After one hour, the mixture was then slowly cooled to room temperature and the precipitate was obtained by centrifugation. The precipitate was also washed with ethanol for three times, then dried and collected as a powder or dispersed in hexane or toluene.

2.3 Characterization Techniques

2.3.1 Powder X-ray Diffraction (XRD)

Powder XRD is a common technique used to characterize the crystal structure of materials. XRD patterns of all samples will be collected with an INEL XRD diffractometer with position-sensitive detector and monochromatic Cu-Kα radiation (λ = 1.5418 Å) in Dr. Holger Kleinke's group in the Department of Chemistry at the University of Waterloo.

Additionally, the size of the crystals can be estimated by the Scherrer equation:

$$L_{hkl} = \frac{k\lambda}{Bcos(\theta)} \quad \text{eq. 2.1}$$

where L_{hkl} is the crystallite size in terms of diameter in nm, k is the dimensionless shape factor, λ is the wavelength of the X-rays, B is the full width at half-maximum (FWHM) of the diffraction peak, and θ is the diffraction angle in radians.

2.3.2 Raman Spectroscopy

Commonly, Raman spectroscopy can be used to detect vibrational modes based on the frequency shift of scattered laser photons. For a solid-state material, Raman spectroscopy can be used to measure the characteristic phonon modes in order to identify the material. Moreover, since different symmetries associated with different crystalline phases can result in different phonon modes, the crystal structure of a material can be further confirmed *via* Raman spectroscopy.

In this research, Raman spectroscopy will be used to detect how the dopant influences the crystallinity of In_2O_3 NCs. Raman spectroscopy measurements will be performed at room temperature with a Renishaw 1000 spectrometer using the Ti-sapphire laser emitting at 785 nm. The employed radiation source uses 10% of the total output power (40 mW). The spectrometer is calibrated using a silicon foil before measurement.

2.3.3 Transmission Electron Microscopy (TEM)

TEM is commonly used to provide information on the morphology of the nanoparticles. A small amount of diluted colloidal IMO NCs or IWO NCs suspension is deposited on copper

grids with lacey Formvar/carbon support films purchased from Ted Pella, Inc. TEM measurements in this project are performed with a JEOL-2010F microscope operating at 200 kV at McMaster University. The ancillary measurement, energy dispersive X-ray (EDX) was performed to analyse the actual elemental composition of the samples. High-resolution TEM (HRTEM) images were analysed by using Gatan Digital Micrograph software.

2.3.4 Ultraviolet-Visible-Near-Infrared (UV-Vis-NIR) Spectroscopy

UV-Vis-NIR spectroscopy can be used to measure the absorption of materials under a wide range of wavelengths. Electronic transitions and optical phenomena at certain wavelengths can be observed.

In this study, UV-Vis-NIR absorption spectra will be carried out with a Varian Carey 5000 UV-Vis-NIR spectrophotometer. Solid-state UV-Vis-NIR measurements are done to avoid the solvent effect in the NIR region through drop-casting the colloidal suspension of IMO NCs onto quartz substrates to form a film. The absorption spectra are collected in the range of 200 nm to 3300 nm.

2.3.5 Fourier Transform Infrared Spectroscopy (FTIR)

FTIR is a technique which can measure the optical properties of different forms of materials in the infrared range. It is a powerful tool to analyse organic molecules based on the characteristic vibration frequencies of certain functional groups. In addition, as the free-carrier LSPR in the doped semiconductor NCs have absorptions in the MIR region, FTIR can also be used to identify these characteristics and contribute to forming the complete absorption spectra

from UV to IR region. KBr pellets with drop-casted colloidal nanocrystals were prepared for FTIR measurements in the range of 400-4000 cm^{-1} on the FTIR Bruker Tensor 37.

2.3.6 X-ray Photoelectron Spectroscopy (XPS)

XPS spectroscopy is a useful technique that can be utilized to determine the composition of samples and the oxidation states of elements in the samples. XPS measurement was performed with a VG Scientific ESCALAB 250 spectrometer using Al Kα radiation (1486.6 eV photon energy) as the excitation source.

2.3.7 Magnetic Circular Dichroism (MCD) Spectroscopy

In this work, MCD measurements are carried out in a Faraday configuration with a Jasco J-815 spectropolarimeter. A variable magnetic field (0-7 T) superconducting magneto-optical cryostat (SM4000-8, Oxford Instruments) with a variable temperature (5-300 K) is applied to samples deposited on strain-free quartz substrates. The full range MCD spectra were collected in the range from 200 to 800 nm with 1 nm data pitch, 1 nm bandwidth, 1 s response time and 1 accumulation. The band gap region MCD spectra were collected from 250-400 nm with a 2 s response time and 2 accumulations.

In addition, the MCD spectra at a variable magnetic field from 0 T to 7 T were collected. Except for the linear fitting of the variable-filed MCD, the spin-only Brillouin function (eq. 2.2) was also used to fit the magnetic field dependence of the exciton MCD intensity in order to distinguish it from the Curie behavior:[64,65]

$$M_S = \frac{1}{2} N g_S \mu_B \left[(2S+1) \coth\left((2S+1) \frac{g_S \mu_B B}{2 k_B T} \right) - \coth\left(\frac{g_S \mu_B B}{2 k_B T} \right) \right] \qquad \text{eq. 2.2}$$

where N is the fitting parameter, S is the spin quantum number, g_S is the corresponding Landé g-factor, B is the external magnetic field, k_B is the Boltzmann constant and T is the temperature. For the fitting, the values g_S = 2.002 and S= 1/2 are used considering the case of free electrons.

Chapter 3. Study of Molybdenum-doped Indium Oxide (IMO) Nanocrystals

3.1 Crystal Structures of IMO NCs

Powder XRD measurements were performed to identify the crystal structure of synthesized IMO NC samples. Figure 3.1 shows the XRD patterns of Mo-doped In_2O_3 (IMO) NCs synthesized at 250 °C with different starting dopant concentrations indicated by the [Mo]/[In] ratios. It can be observed that the XRD patterns of all IMO NCs are in good agreement with the pattern of the bulk bcc-In_2O_3 reference (red vertical lines). Therefore, it can be confirmed that all the IMO NCs maintain the bcc-In_2O_3 structure without the presence of any secondary phases.

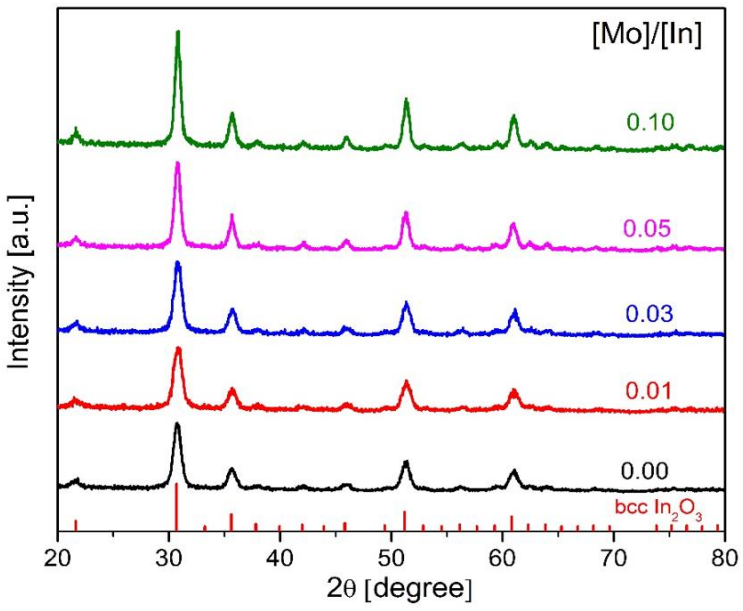

Figure 3.1: Powder XRD patterns of IMO NCs with different initial Mo doping concentrations. The starting concentration ratios of Mo and In precursors ([Mo]/[In]) are indicated in the graph. The red vertical lines correspond to the XRD pattern of bulk bcc-In_2O_3 (JCPDS 06-0416).

In addition, as shown in the Figure 3.1, the XRD peaks tend to be slightly sharper and increase in intensity with higher doping concentrations. According to the Scherrer equation, the diffraction peaks became sharper indicating larger size IMO NCs were formed with increasing doping concentrations. The estimated sizes of NCs with low and high doping concentrations (1% IMO and 10% IMO NCs) obtained from Scherrer equation are 9.4 nm and 14.5 nm, respectively. The nanoparticle size analysis was also measured by TEM for more intuitional and accurate results (see below).

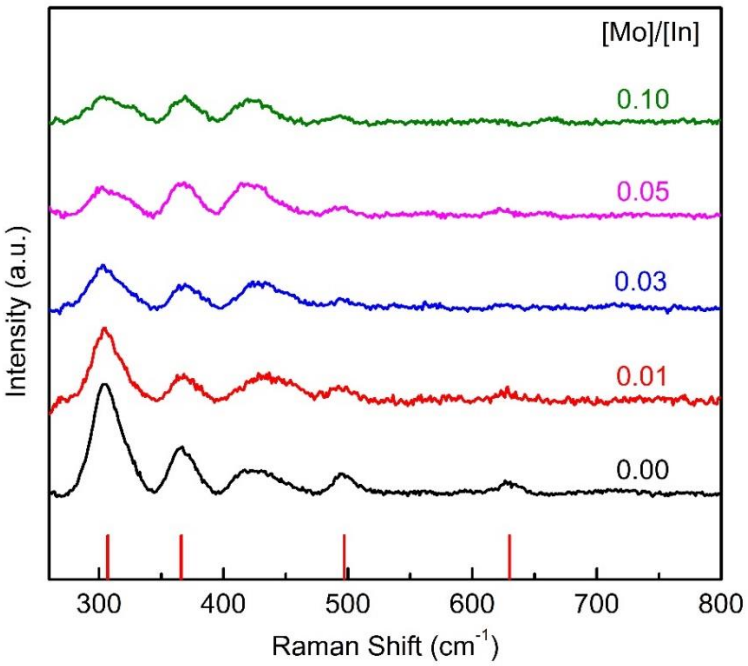

Figure 3.2: Raman spectra of IMO NCs with different Mo doping concentrations. Numbers in the graph show the starting concentration ratios of Mo and In precursors ([Mo]/[In]). The red vertical lines represent the Raman peaks of bulk bcc-In_2O_3.

Raman spectra of IMO NCs with different starting dopant precursor concentrations are shown in Figure 3.2. For the undoped In_2O_3 NCs (black trace), the Raman peaks are in good agreement with the In-O phonon modes reported for bulk bcc-In_2O_3, which are located at 307, 366, 497 and 630 cm^{-1}.[66] The Raman peaks become broader and weaker with increasing [Mo]/[In] starting doping concentrations. Although XRD patterns shown above indicate that all samples retain bcc-In_2O_3 crystal structure, this phenomenon suggests that a local crystal lattice disorder exists in the Mo doped In_2O_3 NCs. The reason might be that the doping of Mo ions causes a decrease in phonon correlation lengths by interstitial or substitutional insertion into the host lattice, and result in nanocrystal lattice disorder.

3.2 Morphology and Elemental Analysis of IMO NCs

To study the morphology and analyse the final doping concentration of Mo in the IMO NCs, TEM measurements were performed for the colloidal samples. The representative TEM images of 1 % and 10 % Mo-doped In_2O_3 NCs are shown in Figure 3.3 and Figure 3.4. In the low doping concentration IMO samples, the overview TEM image in Figure 3.3 (a) shows that most of the nanoparticles exhibit a bipyramid shape, and a fraction of the nanocrystals show a quasi-spherical shape. From the two HRTEM images in Figure 3.3 (b) and 3.3 (c), the measured lattice spacings are 2.90 Å and 4.12 Å, which correspond to the (222) and (211) planes of bulk bcc-In_2O_3, respectively. These results also confirm the bcc-In_2O_3 crystal structure of the colloidal IMO NCs. The size distribution of 1% IMO NCs is shown in the Figure 3.3(d), and the average size is 10.3±1.6 nm, which is in good agreement with the calculated value obtained from the XRD pattern by the Scherrer equation.

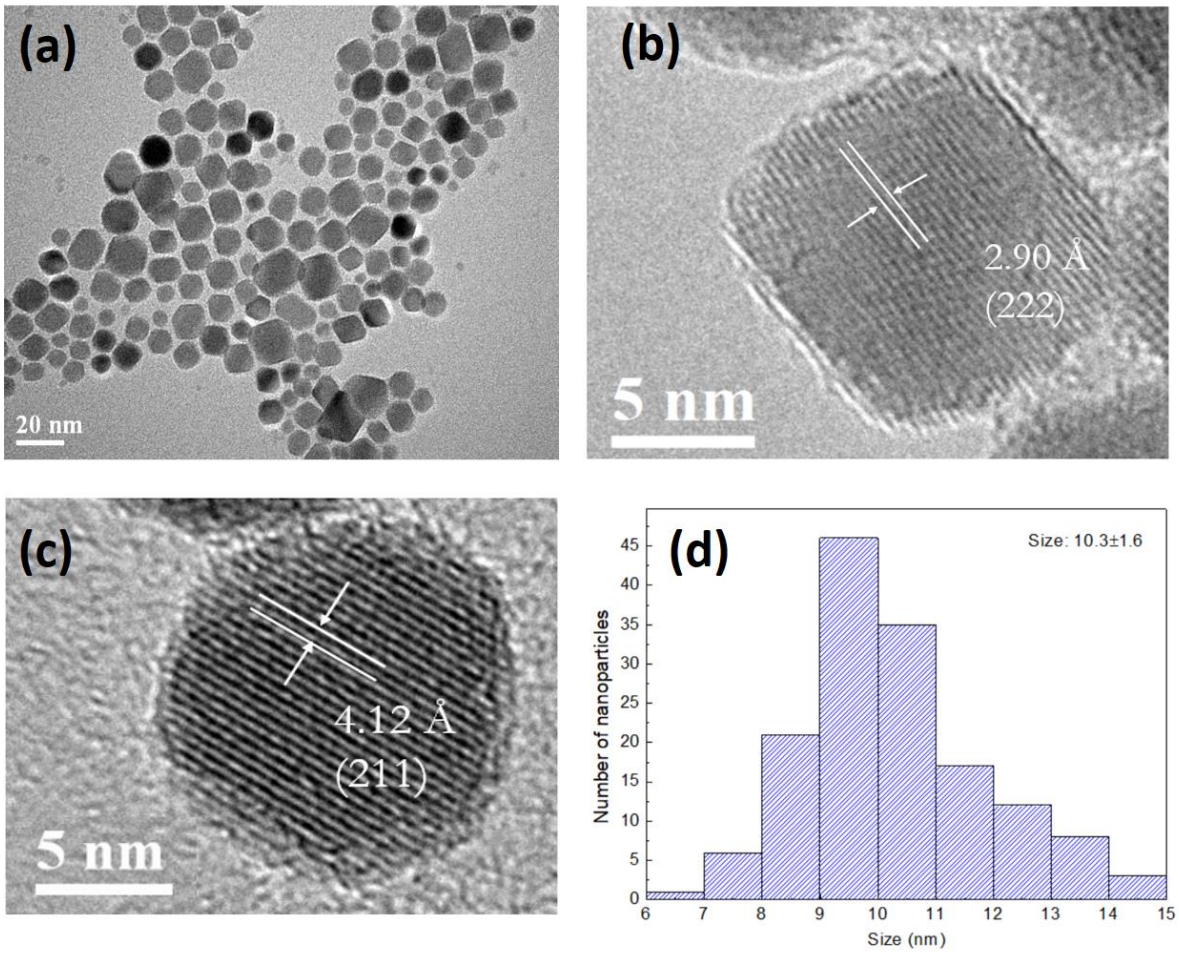

Figure 3.3: Representative TEM images of IMO NCs with starting doping concentration [Mo]/[In]=0.01. (a) Overview TEM image of IMO NCs. (b) and (c) HRTEM images of a single IMO nanocrystal with measured lattice spacing. (d) Size distribution of IMO NCs.

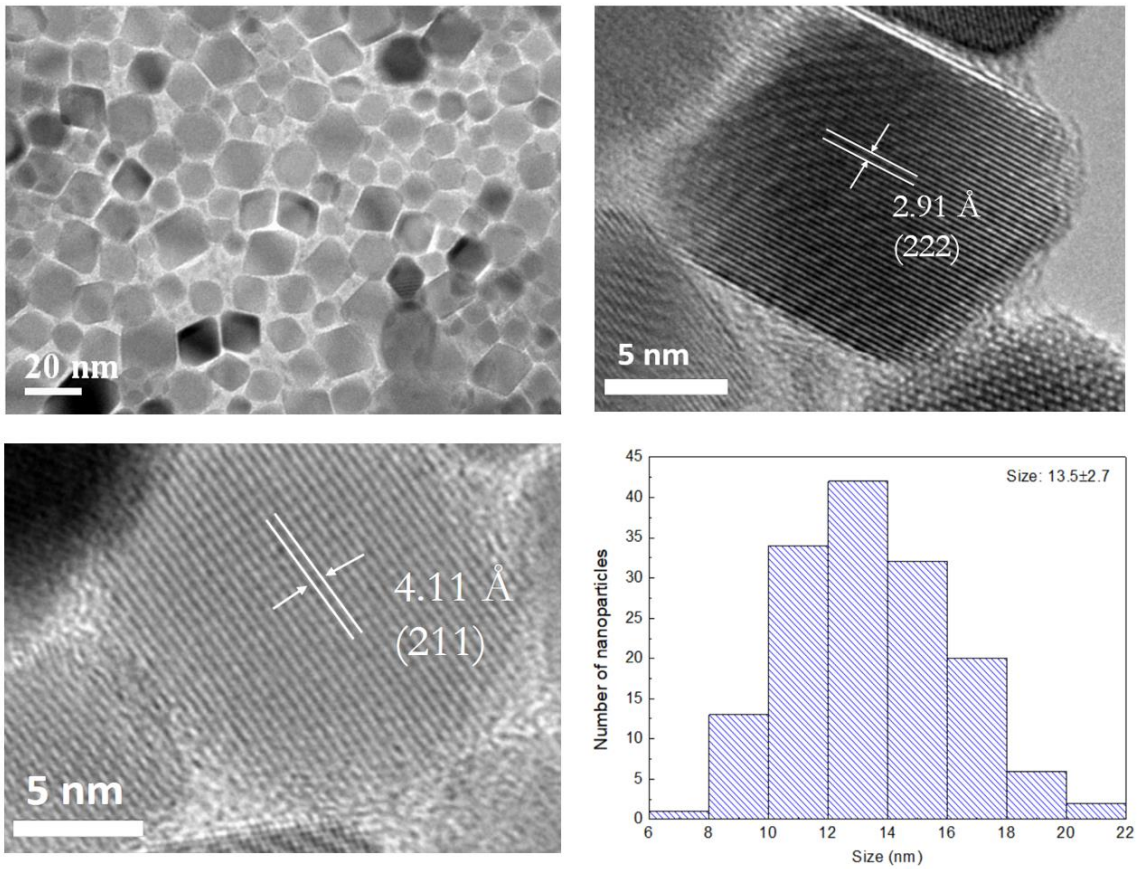

Figure 3.4: Representative TEM images of IMO NCs with starting doping concentration [Mo]/[In]=0.10. (a) Overview TEM image of IMO NCs. (b) and (c) HRTEM images of a single IMO nanocrystal with measured lattice spacing. (d) Size distribution of IMO NCs.

Figure 3.4 shows the TEM results of 10% IMO NCs which has higher doping concentration. It can be observed that in 10% IMO colloidal NC samples, most of the nanocrystals exhibit a bipyramid shape with a relatively broad size distribution. The measured lattice spacings are 2.91 Å and 4.11 Å, which also correspond to the (222) and (211) planes of bcc-In_2O_3, respectively. Compared to the size of 1% IMO NCs, the statistical analysis shows the average size of 10% IMO NCs is relatively larger (13.5±2.7 nm).

Table 3.1: Summary of actual doping concentration of Mo in IMO NCs from EDX and average size of each IMO NCs.

Starting doping ratio [Mo]/[In] （%）	**Mo concentration in IMO NCs （%）**	**Average size (nm)**
1	0.3	10.3
3	1.4	11.1
5	4.2	12.7
10	9.2	13.5

Table 3.1 shows the final concentration of Mo in the doped NC samples obtained from the EDX measurements. It can be observed that the final doping concentration of Mo in each IMO NC sample is systematically lower than the starting doping ratios. However, considering the difference between the starting and final doping concentration, it is reasonable to believe that Mo-doped In_2O_3 NCs have a high doping efficiency. In addition, the average size of IMO NCs also increases with the increasing doping concentrations which is identical to the trend shown in XRD patterns.

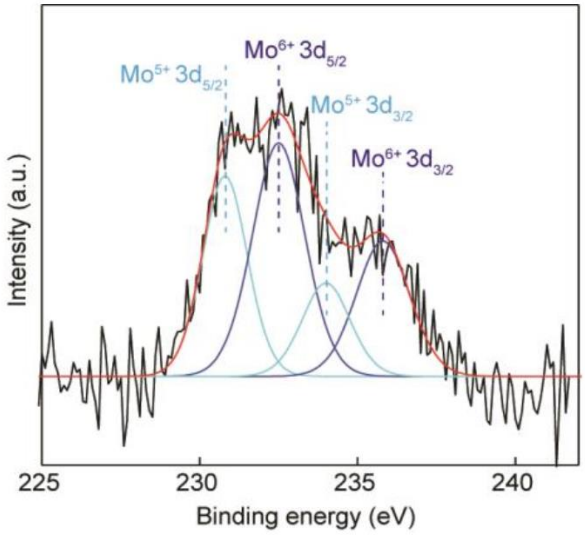

Figure 3.5: Representative molybdenum 3d XPS spectrum of IMO NCs with the synthesized doping concentration [Mo]/[In]= 0.10.[52]

The oxidation state of Mo ions in IMO NCs, which is important for aliovalent doping and the plasmonic and magnetoplasmonic properties, was explored by XPS shown in Figure 3.5. The doublet at 232.5 and 235.8 eV correspond to the Mo^{6+} $3d_{5/2}$ and $3d_{3/2}$, respectively. The peaks at 230.8 and 234.0 eV can be assigned to the Mo^{5+} $3d_{5/2}$ and $3d_{3/2}$, respectively. As shown in the figure, the fitted Gaussian peaks suggested the co-existence of two Mo oxidation states, Mo^{6+} and Mo^{5+}, in the IMO NCs. Similar phenomenon has been reported in Mo-doped TiO_2 that Mo^{6+} and Mo^{5+} were also detected after doped with $MoCl_6$.[67] However, it is difficult to calculate the amount of Mo ions in each oxidation state because of the noise which might be caused by the surface ligands around the IMO NCs.

3.3 Spectroscopic Studies of IMO NCs

3.3.1 UV-Vis-NIR Absorption Spectra of IMO NCs

Solid state IMO NCs were measured in the range from 200 nm to 3300 nm by the UV-Vis-NIR spectroscopy. Figure 3.6 and Figure A1 shows the UV-Vis-NIR absorption spectra of IMO NCs with different Mo doping concentrations. As it can be noticed, each spectrum exhibits a shoulder at around 300 nm, which can be assigned to the band gap absorption of In_2O_3.

To quantitatively compare the plasmon resonance absorption in the NIR region, all the spectra were normalized to the band gap absorption. For the pure In_2O_3 sample, there is no obvious LSPR absorption in the UV-Vis-NIR absorption spectra. However, for IMO NCs with doping ratio [Mo]/[In] up to 0.10, it can be observed that the LSPR absorption increases with the increasing doping concentration. The stronger LSPR absorption indicates that higher free electron concentration was generated with the increasing [Mo]/[In] doping ratio. However, further increase in doping concentration shows that a decrease of LSPR absorption might due to the trapping sites around Mo or the electrons scattering effects.[28,68]

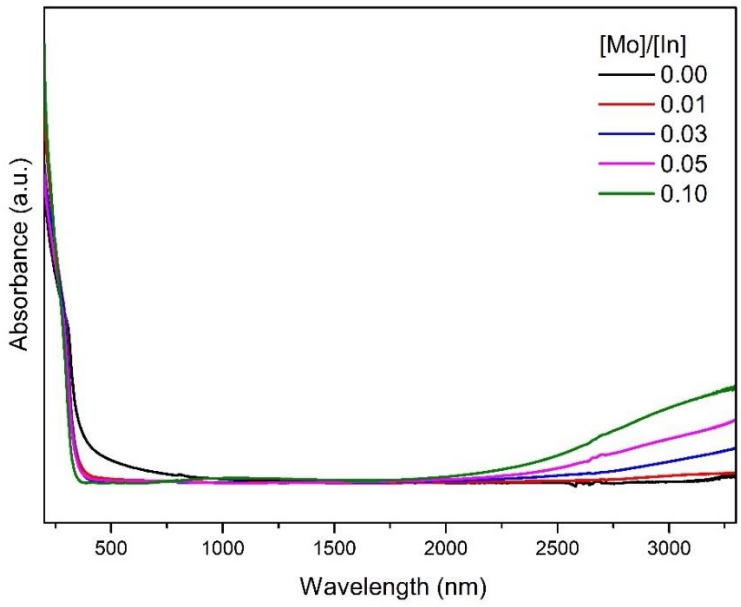

Figure 3.6: Band gap normalized UV-Vis-NIR absorption spectra of IMO NCs with different starting doping concentration ratios ([Mo]/[In]) indicated in the graph.

Figure 3.7 is the Tauc plot of IMO NCs that is obtained from the UV-Vis absorption spectra based on the linear fit of $(\alpha h\nu)^2$ versus the photon energy ($h\nu$). The optical band gap determined by linear extrapolation of pure In_2O_3 NCs is 3.70 eV, which is in a good agreement of the value reported in literature (3.75 eV)[10], and the 10% IMO NCs has the largest "apparent" band gap energy, which is 3.92 eV. With the increasing Mo doping concentrations, obvious blue-shift of the spectra can be observed, which indicate the enlargement of the optical band gap. The phenomenon that the apparent band gap shifts to higher energy can be attributed to the Burstein-Moss effect, which arises from the increased occupancy of conduction band states.[28]

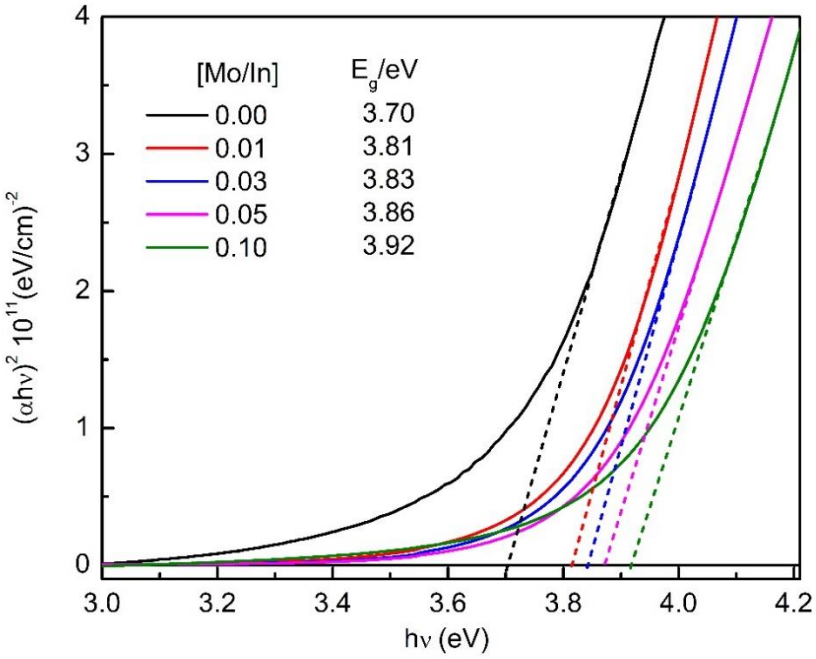

Figure 3.7: Tauc plot of IMO NCs with different doping concentrations showing blue-shift of the optical band gap with indicated band gap values in the inset.

3.3.2 FTIR Absorption Spectra of IMO NCs

The UV-Vis-NIR absorption spectra above show that the LSPR absorption should be continued in the IR region. Therefore, FTIR measurements were performed to further characterize the free electron oscillations. FTIR absorption spectra of the IMO NCs samples are shown in Figure 3.8. Four sharp characteristic peaks at around 603, 564, 538 and 455 cm^{-1} are referred to the In-O phonon vibration modes, which are the characteristic of bcc-In_2O_3.[69] All the FTIR absorption spectra were normalized to the peak centered at 564 cm^{-1} for the purpose of quantitative comparison.

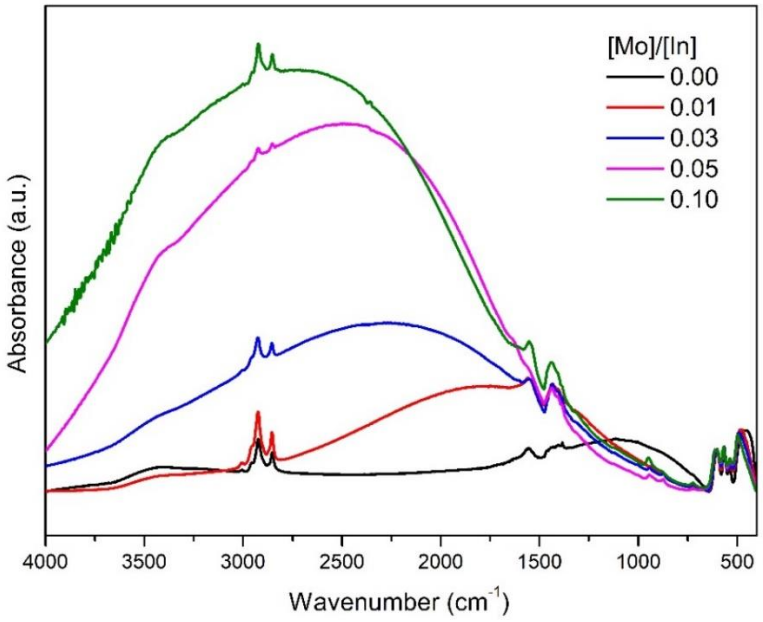

Figure 3.8: Normalized FTIR absorption spectra of IMO NCs with different starting doping concentration ratios ([Mo]/[In]) indicated in the graph.

As shown in the Figure 3.8, there is dramatically different spectra between the pure In_2O_3 NCs and the molybdenum-doped samples, especially for the high doping concentrations. For the undoped In_2O_3 NCs, there is a small bump absorption at around 1000 cm^{-1}. This weak LSPR absorption might be attributed to the free electron resonance that is generated from the oxygen vacancies in the lattice.[70] For the IMO NCs, broad and strong LSPR absorption bands can be found from 4000 cm^{-1} to 646 cm^{-1} due to the surface plasmonic resonance of free carriers excited by the MIR light source. The trend of IMO NCs LSPR absorption in the FTIR spectra is consistent with the one in change in the UV-Vis-NIR spectra. The intensity of plasmon resonance absorption gradually increases with the increasing doping concentration. Moreover, a blue-shift can also be observed in the spectra when the Mo doping level is increased, which indicates the

increasing LSPR peak energy. The increase in both LSPR intensity and energy suggest that higher free electron concentrations are achieved through the aliovalent doping.

In addition, two intense peaks at 2923 cm^{-1} and 2850 cm^{-1} can be assigned to the asymmetric CH_2 stretch and symmetric CH_2 stretch of oleic acid which is used for the surface treatment in the post-synthetic procedure. The other two peaks at 1555 cm^{-1} and 1441 cm^{-1} are the characteristic of asymmetric (COO−) and symmetric (COO−) stretch which are also contributed to the oleic acid.[69] The appearance of the IR absorption arises from organic functional groups suggesting that the synthesized nanocrystals have been successfully coated with oleic acid.

Since the plasmon resonance absorption appears in both UV-Vis-NIR and FTIR absorption spectra, these two different optical spectra were merged together based on the overlapping region from 2500 to 3300 nm to obtain the complete absorption band of LSPR. Figure 3.9 shows the normalized absorption spectra of IMO NCs with different Mo doping concentrations up to 10 % in the units of electron volt. The whole plasmon resonance absorption and its characteristics are distinctly presented in this figure. With the increasing doping concentration of molybdenum precursor, the plasmon absorption increases in intensity as well as the LSPR band energy. It demonstrates that plasmonic properties have been introduced into the In_2O_3 host lattice through the doping with molybdenum ions. Specially, the plasmon resonance can be tuned in certain range by varying the doping concentration which enable more flexibility in the applications of the IMO NCs.

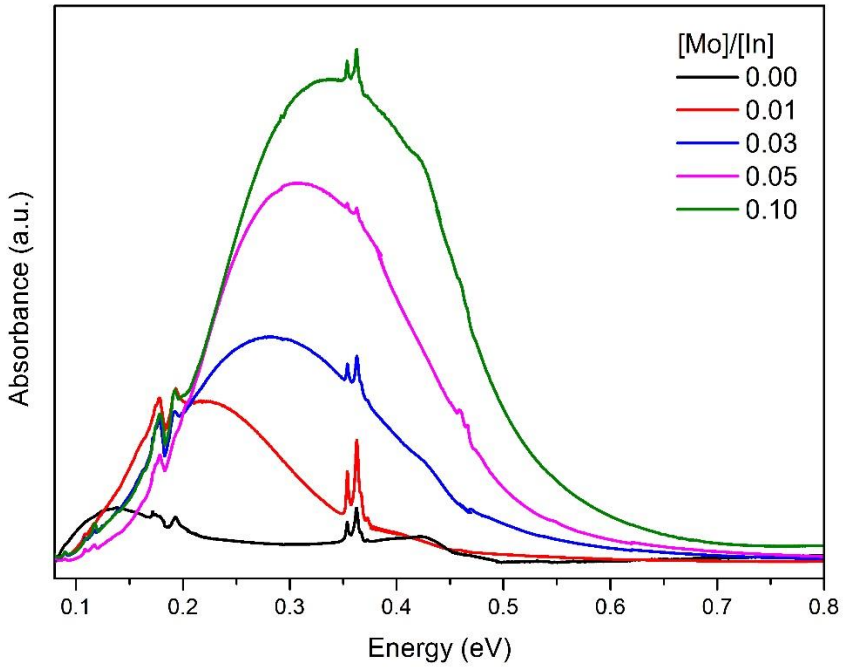

Figure 3.9: Normalized LSPR absorption spectra of Mo-doped In_2O_3 NCs in the range from NIR to MIR in energy. Different starting doping concentration ratios ([Mo]/[In]) are indicated in the graph.

The trend of the LSPR is consistent with the prediction from the Drude–Lorentz model. The free electron carrier concentration in the IMO NCs can be estimated based on the eq. 1.2 with the optical parameters for bulk bcc-In_2O_3 (m^*=0.3m_0, ε_{opt} =4.0). The calculated results are shown in the following Table 3.2.

Table 3.2: Summary of estimated free electron concentrations of the IMO NCs based on the Drude-Lorentz model.

Actual [Mo]/[In] in IMO （%）	**Free electron concentration N (cm^{-3})**
0.3	3.8×10^{19}
1.4	6.8×10^{19}
4.2	8.4×10^{19}
9.2	1.1×10^{20}

3.4 Magnetoplasmonic properties of IMO NCs

It has been reported that MCD spectroscopy can be used as a powerful probe of the LSPR of noble metal nanoparticles and doped semiconductor nanocrystals.[62,71] Therefore, to explore the magnetoplasmonic properties of IMO NCs, MCD measurements were carried out. In Figure 3.10 (a), the top part shows the absorption spectrum of 1 % IMO NCs at 5 K, and the bottom part shows MCD spectra of 1 % IMO NCs at variable external magnetic field strengths which were also collected at 5 K. The MCD spectra with a negative maximum at around 3.93 eV coincide with the band-edge absorption. Figure 3.10 (b) shows that the MCD intensity is linearly dependent on the magnetic field, which is consistent with the relationship reported for MCD intensity of LSPR.[62] The Brillouin function is fit to the same experimental data points as well, and the significant deviation can be observed from the fitting. The results confirm that the linear field dependence of MCD signal is not related to the Curie-type paramagnetism but arises from the Zeeman splitting of the band states which is caused by plasmon-exciton coupling.

The 7 T MCD spectra of the nanocrystals in the same band gap region collected at different temperatures from 5 K to 300 K are shown in Figure 3.10 (c). With the increasing temperature, the MCD intensity rapidly drops at first up to 50 K and then levels off. The temperature dependence of MCD intensity is shown in Figure 3.10 (b), and the data points were fit to Curie's law. When the temperature reached 300 K, about 75% of the MCD intensity remained. A temperature dependence of MCD intensity is characteristic for the C term MCD, which indicates the Zeeman splitting of the ground states while at room temperature only A term MCD intensity remained due to the temperature independence. Generally, the C term MCD can be observed in material with ground-state paramagnetism and followed by a Curie-type temperature dependence. It has been demonstrated that there is no temperature dependence for MCD intensity of LSPR up to 30 K, and the excitonic MCD intensity of ITO is also temperature independent up to room temperature.[52,62]

The Curie-type temperature dependence observed in 1 % IMO NCs account for the presence of Mo dopant in the +5 oxidation state, which is reduced from the Mo^{6+} precursors. Similar reduction reactions have been found in MoO_{3-x} NCs and Mo doped TiO_2 NCs.[67,72] Although the MCD intensity decreased and followed Curie behaviour when temperature increased, the majority of the intensity maintained at room temperature. These results indicate that A-term MCD is dominant in IMO NCs which is related to the plasmon-exciton coupling.

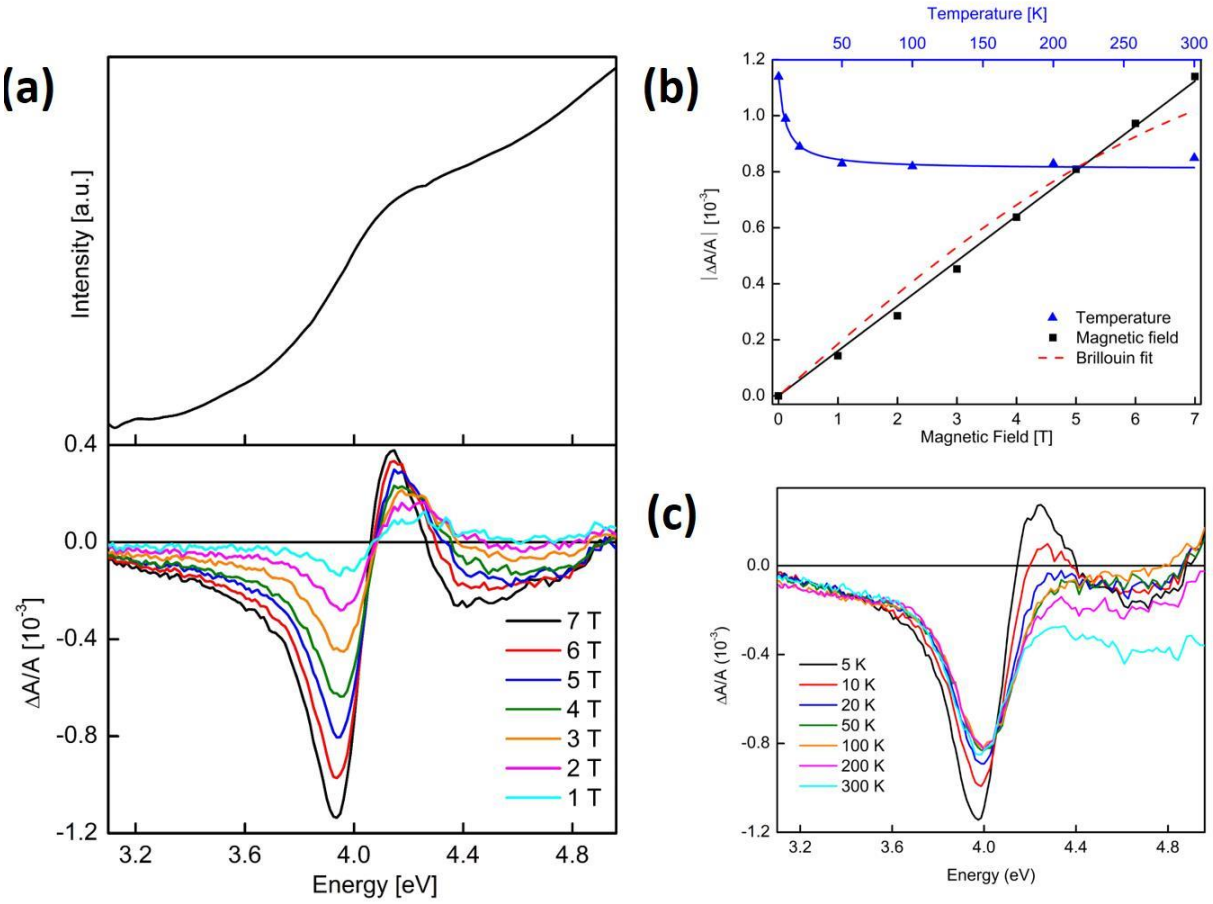

Figure 3.10: (a) Absorption (top) and MCD (bottom) spectra of IMO NCs with starting doping concentration [Mo]/[In]=0.01 collected at 5 K. MCD spectra collected at different external magnetic field strengths are indicated in the graph. (b) Magnetic field (black data points) and temperature (blue data points) dependence of MCD intensity recorded at 3.93 eV for IMO NCs in (a) and (c). Black solid line and red dashed line are the linear and Brillouin function fit to the black data points, respectively. Blue solid line is fit to the Curie's law of blue data points. (c) The MCD spectra at 7 T of IMO NCs in (a) are collected at different temperatures from 5 K to 300 K.

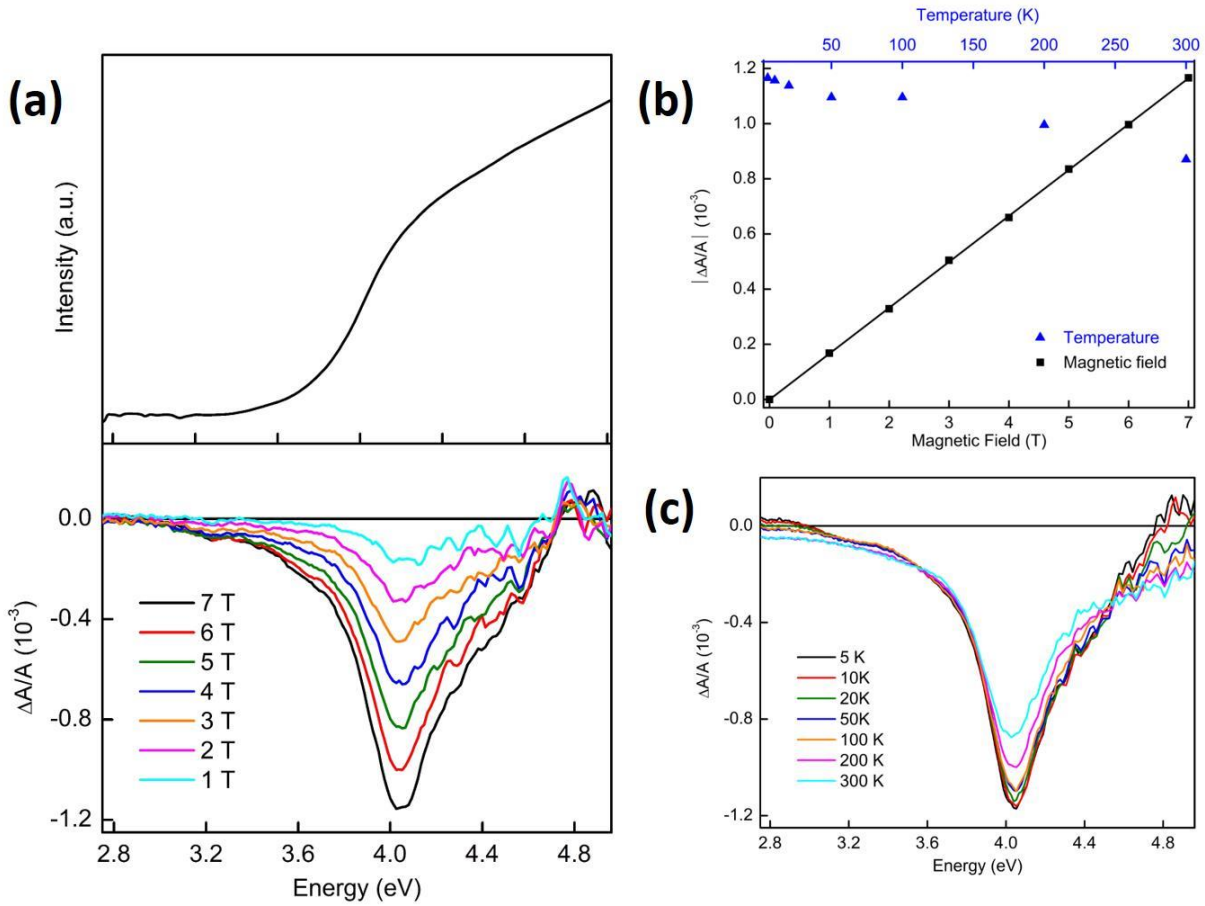

Figure 3.11: (a) Absorption (top) and MCD (bottom) spectra of IMO NCs with starting doping concentration [Mo]/[In]=0.10 collected at 5 K. MCD spectra collected at different external magnetic field are indicated in the graph. (b) Magnetic field (black data points) and temperature (blue data points) dependence of MCD intensity recorded at 4.03 eV for IMO NCs in (a) and (c). Black solid line is the linear function fit to the black data points. (c) The 7 T MCD spectra of IMO NCs collected at different temperatures (5 K to 300 K).

The MCD spectra of 10% IMO NCs are summarized in Figure 3.11. The MCD spectra are dominated by negative band which coincides with the band gap absorption. Blue shift of the

band gap absorption and MCD maximum are consistent with the phenomenon shown in Tauc plot. The maximum MCD intensity at 4.03 eV also shows linear relationship with the applied magnetic field which is associated with plasmon-exciton coupling. The MCD signal slightly decreased with increasing temperature due to the presence of Mo^{5+}. However, compared to 1 % IMO NCs, intense MCD intensity persisted at low temperature because of the stronger LSPR in 10 % IMO NCs, which results in a stronger plasmon-exciton coupling.

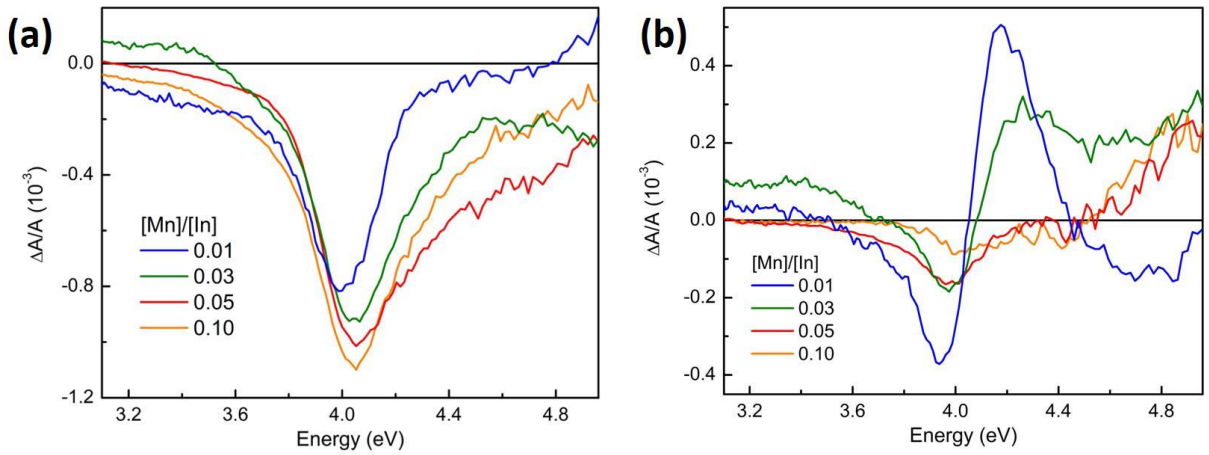

Figure 3.12: (a) Normalized A term MCD spectra of IMO NCs with different doping concentrations collected at 100 K. (b) Normalized C term MCD spectra of IMO NCs with different Mo doping concentrations.

Figure 3.12 (a) shows the A-term MCD spectra of IMO NCs with various doping concentrations, and all spectra were collected at 100 K with the same band gap absorbance. The MCD spectra collected at low temperature 5 K are thought to be the combination of the A-term and C-terms MCD signals. However, the MCD signal at 100 K only involves Zeeman splitting of the degenerate excited states which results in the temperature independent A-term MCD

spectra. It can be observed that at this high temperature, the remaining MCD intensity increased with the increasing amount of Mo dopants.

On the contrary, the C term MCD spectra presented in Figure 3.12 (b) shows the exactly opposite trend. The C term intensity results from the difference between the MCD intensity collected at 5 K and 100 K, and the contribution of C term MCD decreased with the increasing doping concentrations. Therefore, since the strength of plasmon-exciton coupling increases with increasing doping concentrations, the relative contribution of the A term intensity increases while the C term intensity decreases. These results demonstrate that with the help of cyclotron magnetoplasmonic modes, the control of the magnitude and orientation of charge carrier polarization can be achieved.[52]

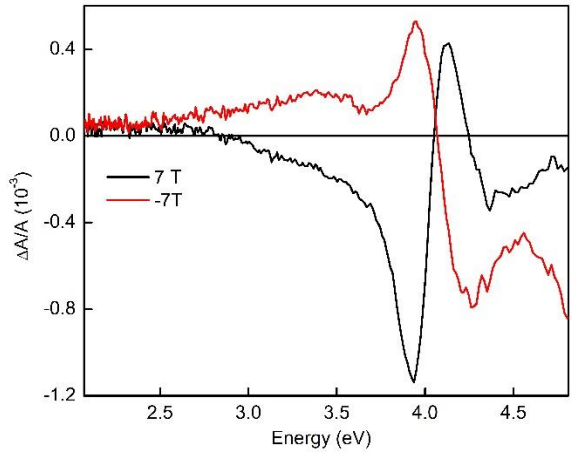

Figure 3.13: Exciton MCD spectra of 1% IMO NCs collected at 5 K under the opposite polarities of the external magnetic fields.

Figure 3.13 shows the MCD spectra of IMO NCs recorded at the opposite external magnetic fields of 7 T. Reversed exciton MCD signal can be observed when the magnetic field changes into negative 7 T, which indicates the full manipulation of charge carrier polarization through changing the direction of the cyclotron motion of free electrons.

The plasmon-induced carrier polarization as the results shown above is an interesting and fascinating phenomenon. However, there are still some challenges remain in explaining the mechanism of this process since the excitonic transitions and LSPR oscillations are off-resonant and the LSPR is not excited directly in these MCD measurements. Additionally, there are two types of coupling, the exciton-phonon coupling and plasmon-phonon coupling, have been widely reported and studied in different semiconductor nanocrystals.[73–75] Therefore, one possible and reasonable hypothesis is that the optical phonons, which can couple with both plasmons and excitons, generate a phonon-mediated coupling mechanism during this process.[52] More importantly, the optical phonons can transfer angular momentum as well, which makes the generation of the magnetoplasmonic modes and the splitting of the band states in an external magnetic field plausible.[52,76]

Chapter 4. Study of Tungsten-doped Indium Oxide (IWO) Nanocrystals

4.1 Crystal Structures of IWO NCs

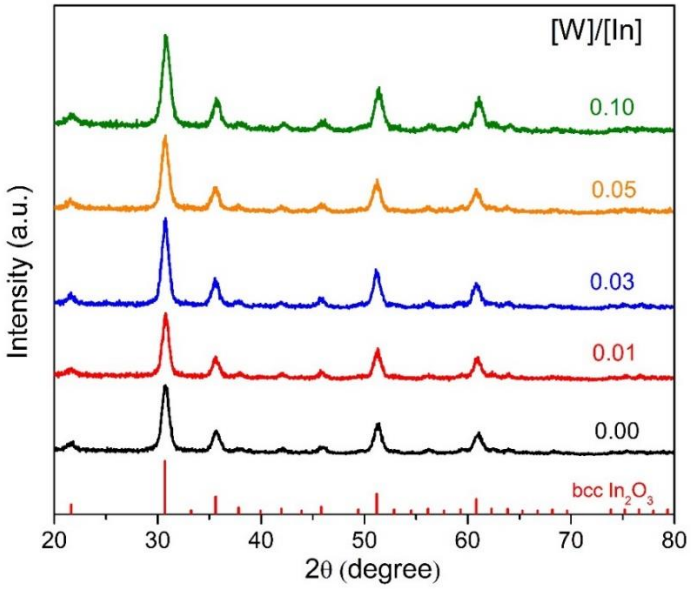

Figure 4.1: Powder XRD patterns of IWO NCs with different initial W doping concentrations. The starting concentration ratios of W and In precursors ([W]/[In]) are indicated in the graph. The red vertical lines correspond to the XRD pattern of bulk bcc-In_2O_3 (JCPDS 06-0416).

The powder XRD patterns of as-synthesized IWO NCs with different doping concentrations are presented in Figure 4.1. Similar to Mo-doped In_2O_3 NCs, all the IWO NCs are well-crystallized, and the patterns are in good agreement with the reference of bulk bcc-In_2O_3. The absence of other diffraction peaks indicates no secondary phases in the IWO NCs and all the samples maintain the expected crystal structure.

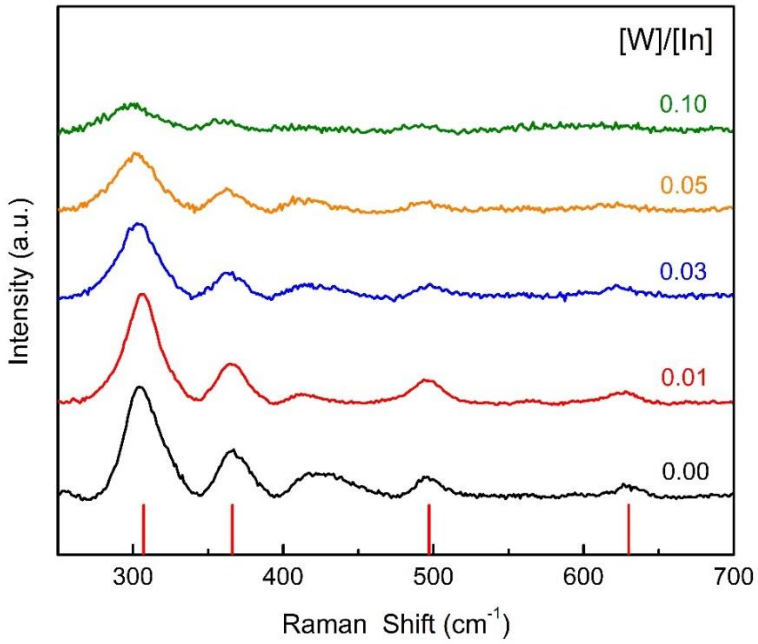

Figure 4.2: Raman spectra of IWO NCs with different W doping concentrations. Numbers in the graph show the starting concentration ratios of tungsten and indium precursors ([W]/[In]). The red vertical lines represent the characteristic Raman peaks of bulk bcc-In_2O_3.

Figure 4.2 shows the Raman spectra of IWO NCs with different starting doping concentrations which provide a deeper insight into the crystal structures. For the low doping ratios, the Raman peaks of IWO NCs match well with the characteristic In-O phonon modes of bulk bcc- In_2O_3. With the increasing doping concentrations, however, continuous weakening and broadening of the characteristic peaks can be observed. Particularly, the Raman peaks at 497 and 630 cm^{-1} almost disappear for the IWO NCs with high doping concentration ([W]/[In]=0.10). The results shown in the Raman spectra imply the distortion of the local crystal lattice also exists in the W-doped In_2O_3 NCs.

4.2 Morphology and Elemental Analysis of IWO NCs

TEM images were collected to investigate the morphology and measure the lattice fringes of the synthesized IWO NCs. As shown in Figure 4.3 (a), most 1% IWO nanoparticles exhibit a bipyramid shape which is more distinct in the HRTEM image. In addition, from the HRTEM image Figure 4.3 (b), the lattice spacings were measured to be 4.12 Å and 2.91 Å, which correspond to the (211) and (222) planes of bulk bcc-In_2O_3, respectively. The average size of 1 % IMO based on statistical analysis is about 7.5 nm.

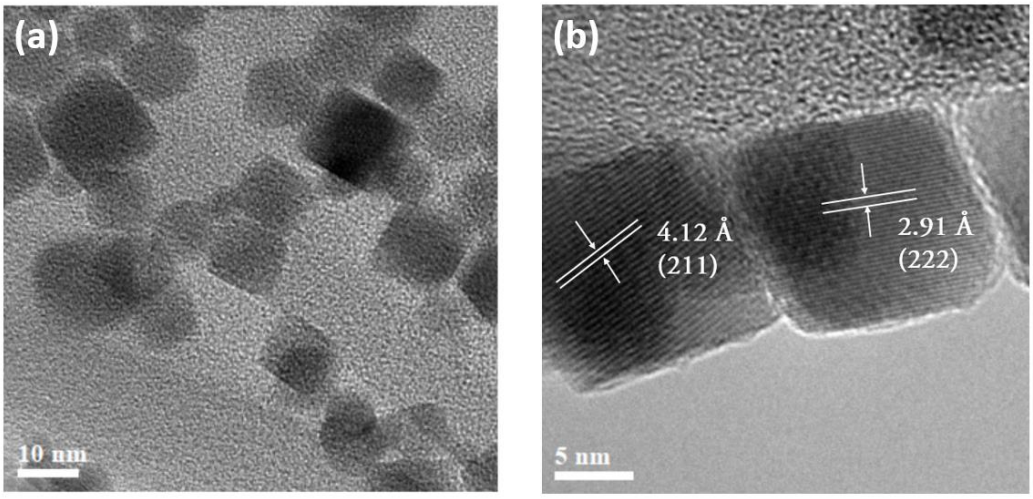

Figure 4.3: Representative TEM images of IWO NCs with starting doping concentration [W]/[In]=0.01. (a) Overview TEM image of IWO NCs. (b) HRTEM image of nanoparticles with measured lattice spacing.

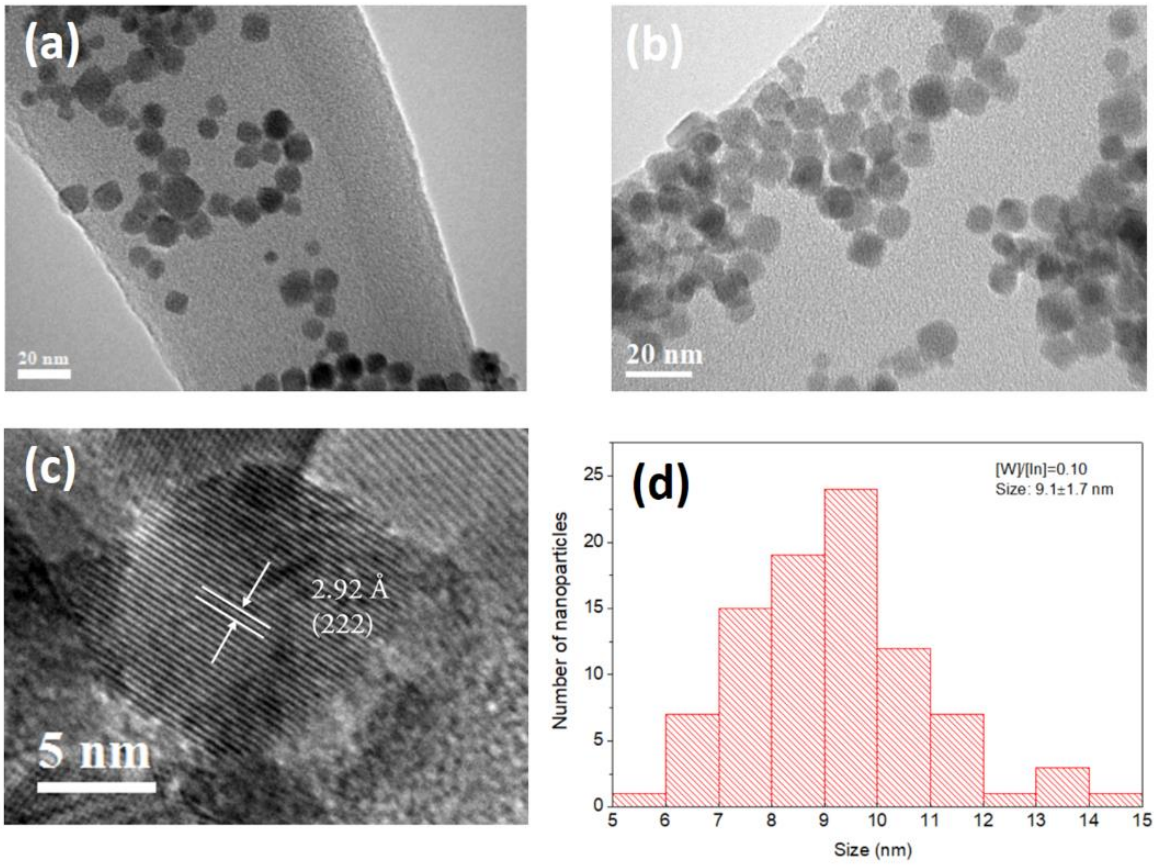

Figure 4.4: Representative TEM images of IWO NCs with starting doping ratio [W]/[In]=0.10. (a), (b) Overview TEM images of IWO NCs. (c) HRTEM image of a single nanoparticle with measured lattice spacing. (d) Size distribution of IWO NCs.

Figure 4.4 shows the IWO NCs with high tungsten doping concentration. The overview TEM images also indicate the bipyramid shape of IWO nanoparticles. The lattice spacing about 2.92 Å for 10 % IWO NCs obtained from HRTEM image is consistent with the (222) plane of bulk bcc-In_2O_3 and further demonstrates the colloidal IWO NCs maintain the expected crystal structure. The size distribution of the sample is illustrated in Figure 4.4 (d), and the average size is around 9.1±1.7 nm.

4.3 Spectroscopic Studies of IWO NCs

4.3.1 UV-Vis-NIR Absorption Spectra of IWO NCs

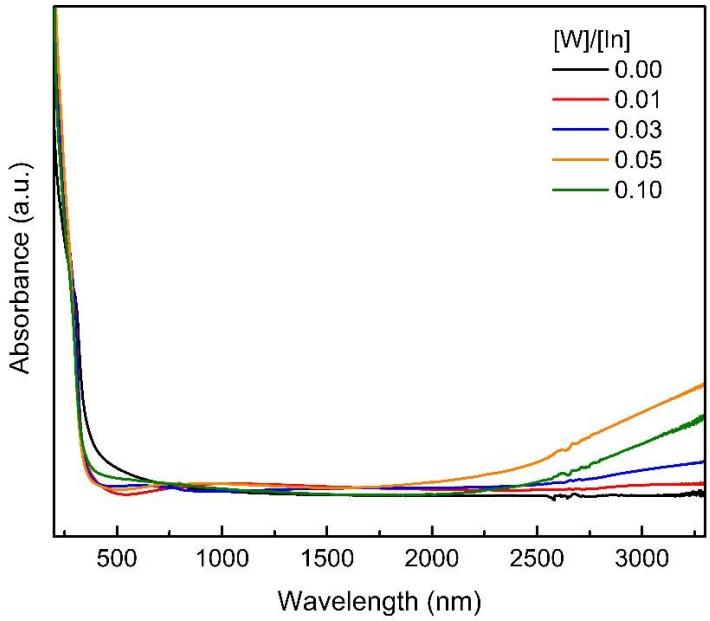

Figure 4.5: Band gap normalized UV-Vis-NIR absorption spectra of IWO NCs with different starting doping concentration ratios ([W]/[In]) indicated in the graph.

Figure 4.5 shows the UV-Vis-NIR absorption spectra of IWO NCs with different doping concentrations up to 10%. All absorption spectra were normalized to the band gap absorption at around 300 nm. As can be observed from the figure, the plasmon resonance of IWO NCs starts to arise at about 2500 nm, and for the 5 % IWO NCs, which exhibits the strongest LSPR absorption in the NIR region, the plasmon resonance starts from 2000 nm. From 1 % to 5 % IWO NCs, the LSPR absorption increased with the increase in the doping concentration. However, a trend reversal occurs in the 10 % IWO NCs, as the weaker intensity of the plasmon resonance is shown in the NIR region which indicates the free electron density decreases when

the doping ratio reaches a limitation. The reason that further increase in doping concentration leads to the decrease of LSPR absorption intensity might be because of the electrons scattering effects of by defects in the lattice or the scattering around the ionized W dopant.[28,68]

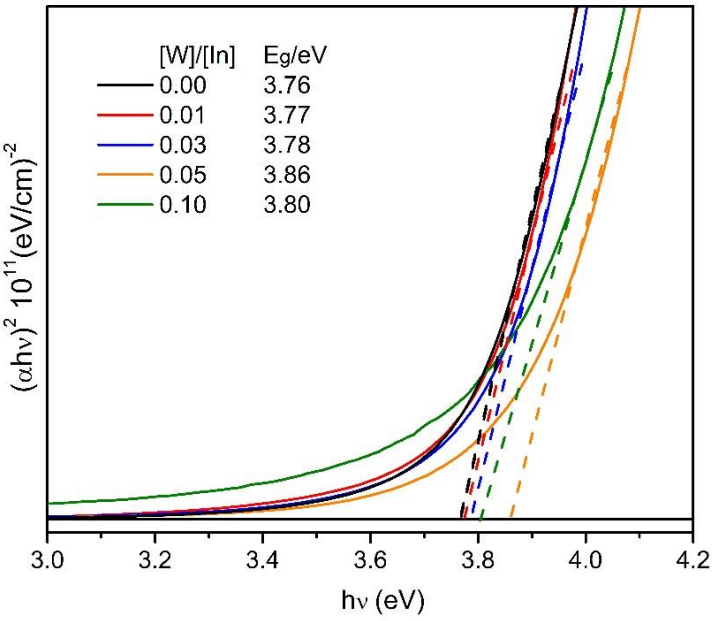

Figure 4.6: Tauc plot of IWO NCs with different doping ratio showing blue-shift of the optical band gap with indicated band gap values in the inset.

The Tauc plot calculated from the UV-Vis-NIR absorption spectra of IWO NCs is shown in Figure 4.6. The optical band gap energy shows the same trend presented in Figure 4.5 that up to 5 % doping, the band gap energy increases with the increasing doping concentrations and then drops back with higher doping concentration. Therefore, 5 % IWO NCs exhibits the largest band gap value which is 3.86 eV and the band gap energy of 10 % shifts back to lower energy level. The blue-shift of the optical band gap can also be referred to as the Burstein-Moss effect, which indicates the increased occupancy of conduction band states. However, a further increase in W^{6+}

concentration leading to the red shift of the spectra suggests the electronic structure dependence on the nanocrystal composition.

4.3.2 FTIR Absorption Spectra of IMO NCs

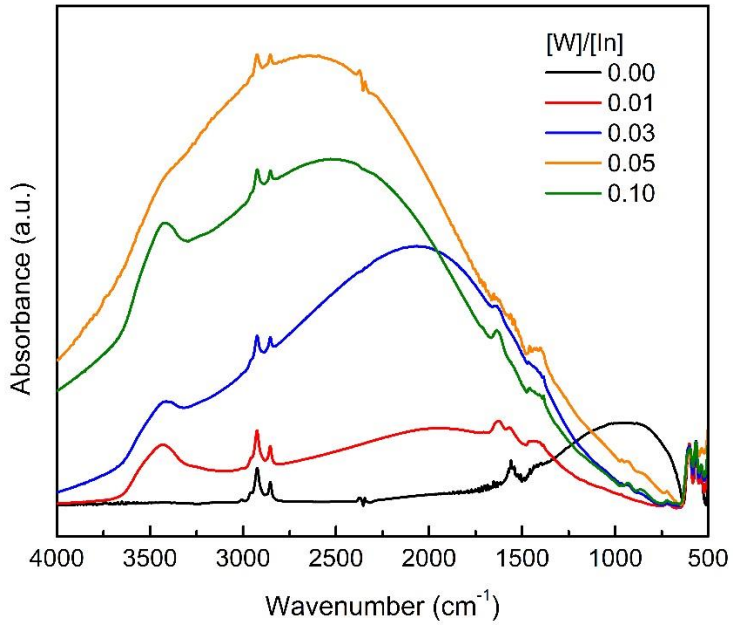

Figure 4.7: Normalized FTIR absorption spectra of IWO NCs with different starting doping ratios ([W]/[In]) indicated in the graph.

Figure 4.7 shows the FTIR absorption spectra of IWO NCs with different doping concentrations in the range from 4000 cm^{-1} to 500 cm^{-1}. To quantitatively compare the plasmon resonance, all the FTIR spectra are normalized to the In-O phonon vibration mode which located at 564 cm^{-1}. In 1 %, 3 % and 10 % IWO NCs, a shoulder appears at around 3300 cm^{-1} which is the O-H stretch coming from the moisture. It is interesting to notice that for the pure In_2O_3 NCs

without any tungsten dopant, there is a small absorption peak from 1500 to 646 cm^{-1}. One reasonable explanation is that the resonance of the delocalized free electrons in the oxygen-deficient lattice results in this absorption band.

Broad plasmon absorption band of the W-doped In_2O_3 samples can be observed in the spectra, and the trend of the LSPR absorption of IWO NCs is identical to the one shown in the UV-Vis-NIR absorption spectra. Specifically, the absorption intensity of the LSPR peaks increasing with the doping concentrations up to 5% W-doped In_2O_3 NCs and drops back for the 10% IWO NCs. In addition, a blue-shift of the plasmon resonance band with the increasing absorption intensity can also be observed in the figure, which implies the increase in the LSPR peak energy as well as the free electron concentrations.

Figure 4.8 shows the normalized LSPR absorption spectra of IWO NCs which obtained from the combination of UV-Vis-NIR spectra and FTIR spectra. Therefore, complete plasmon resonance band can be observed in the figure. The results demonstrated that the plasmon resonance in the In_2O_3 NCs could be readily introduced through the doping of W and altered by varying the doping concentrations. The estimated free electron density of the 5% IWO NCs which has the strongest LSPR is 9.4×10^{19} cm^{-3} according to the Drude–Lorentz model.

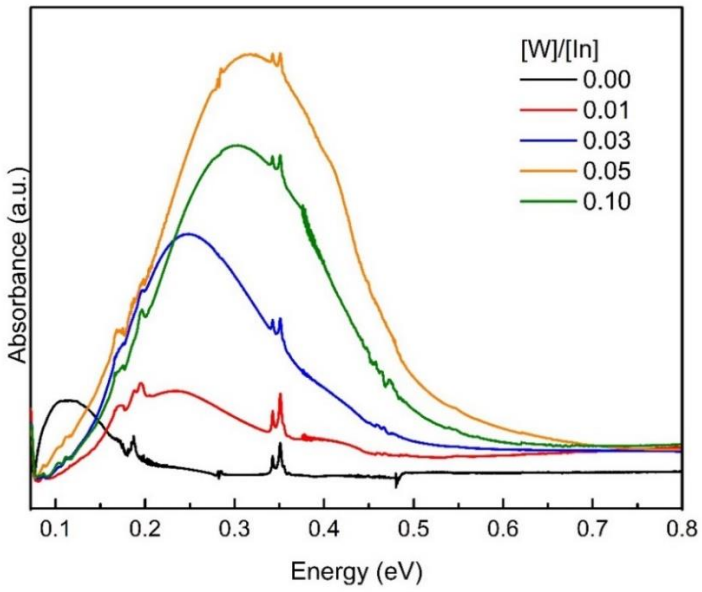

Figure 4.8: Normalized LSPR absorption spectra of IWO NCs in the range from NIR to MIR in the unit of energy. Different starting doping concentration ratios ([W]/[In]) are indicated in the graph.

4.4 Magnetoplasmonic Study of IWO NCs

To further study the magnetoplasmonic properties of the same group elements doped In_2O_3 NCs and explored the generality of the plasmon-induced carrier polarization as well as its manipulation, MCD spectroscopy measurements were performed for the IWO NCs with different doping concentrations as well.

Figure 4.9 (a) shows the absorption spectrum and variable-field MCD spectra of 1 % IWO NCs with the actual doping concentration of 0.40 % recorded at 5 K. The MCD intensity increases with the increasing external magnetic fields, and the relationship between the MCD

band maximum and the magnetic fields are shown in Figure 4.9 (b). It is clear that the MCD intensity starts to saturate at high magnetic fields, which is considered to be a characteristic behavior of paramagnetism. The data points to the coexistence between the Brillouin function and the linear dependence, and the Brillouin fitting seems to dominate in this case, which indicates a sizeable paramagnetism in the 1% IWO NCs. The paramagnetism might originate from the presence of W^{5+} which were reduced from the W^{6+} precursor.

In addition, Figure 4.9 (c) shows the 7 T MCD spectra of the IWO NCs in the same band gap region recorded at different temperature ranges from 5 K to 300 K. It is notable that the MCD intensity decreases rapidly when the temperature slightly increases. However, when the temperature reaches to 50 K which is a relatively high temperature compared to 5 K, the MCD signals start a slow decline. At room temperature approximately 56% of the MCD intensity maintained.

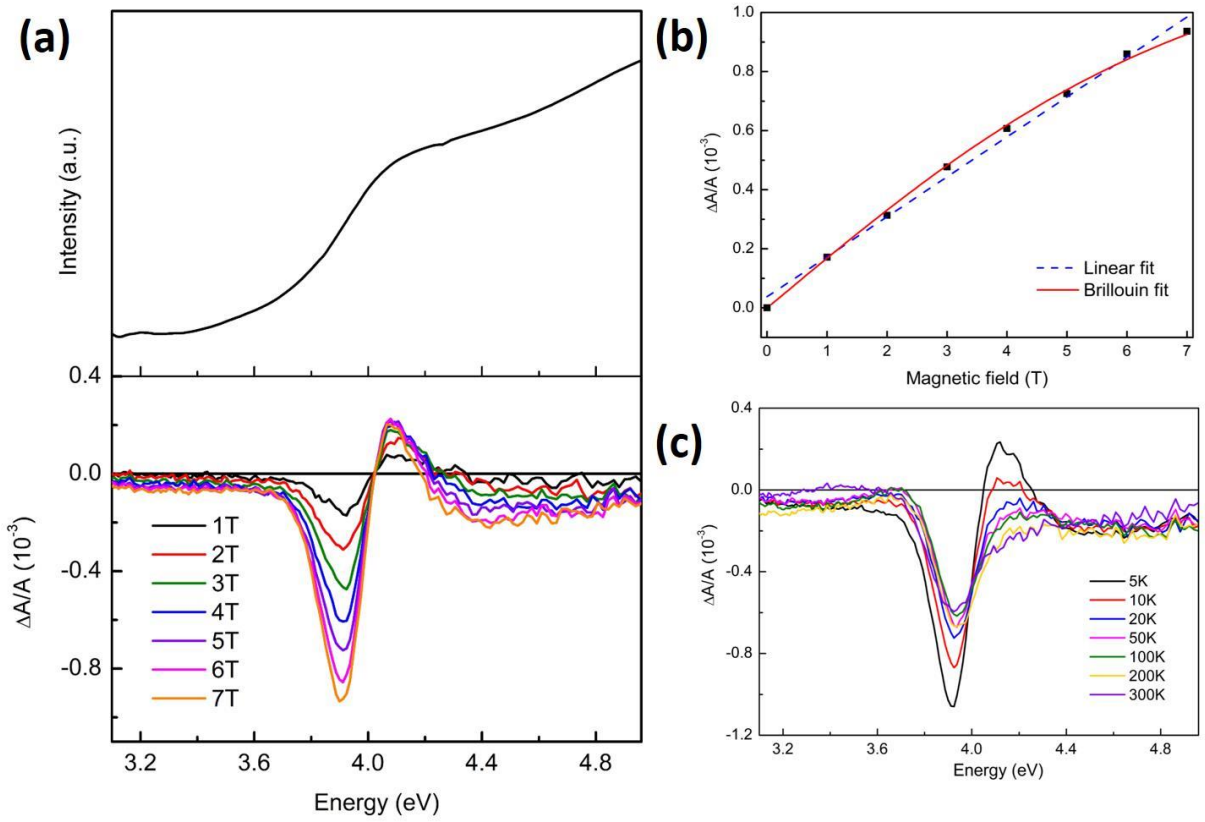

Figure 4.9: (a) Absorption (top) and MCD (bottom) spectra of IWO NCs with starting doping concentration [W]/[In]=0.01 collected at 5 K. MCD spectra collected at different external magnetic field strengths are indicated in the graph. (b) Magnetic field (black data points) dependence of MCD intensity recorded at 3.91 eV for IWO NCs in (a). Red solid line and blue dashed line are the Brillouin and linear function fit to the data points, respectively. (c) The MCD spectra at 7 T of IWO NCs in (a) are collected at different temperatures from 5 K to 300 K.

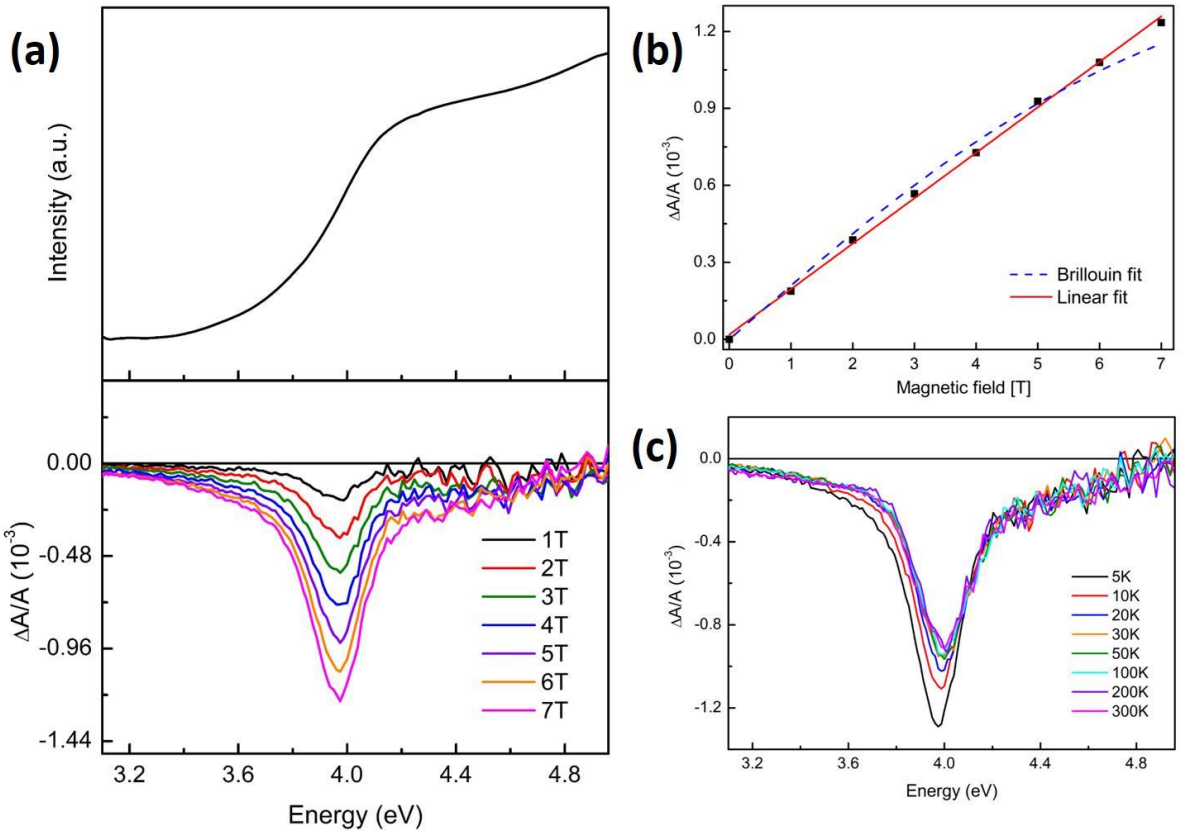

Figure 4.10: (a) Absorption (top) and MCD (bottom) spectra of IWO NCs with starting doping concentration [W]/[In]=0.10 collected at 5 K. MCD spectra collected at different external magnetic field strengths are indicated in the graph. (b) Magnetic field (black data points) dependence of MCD intensity recorded at 3.97 eV for IWO NCs in (a). Red solid line and blue dashed line are the linear and Brillouin function fit to the data points, respectively. (c) The MCD spectra at 7T of IWO NCs in (a) are collected at different temperatures (5 K - 300 K).

Figure 4.10 summarized the same MCD measurement performing on 10 % IWO NCs. The slightly blue shift of the band gap absorption and MCD maximum can be observed in Figure 4.10 (a), which are in agreement with the results shown in the Tauc plot. The MCD spectra are dominated by negative band which are similar to the MCD spectra of 10 % IMO NCs, and the

maximum MCD signals at 3.97 eV show no sign of saturation under high magnetic field, but a linear relationship with the external magnetic fields, which is considered to be the signature of LSPR in doped semiconductor nanocrystals.[62] Variable temperature MCD spectra at 7 T are shown in Figure 4.10 (c). Compared to 1% IWO NCs, more MCD signal remains at low temperature, and when increased to room temperature, about 71% MCD intensity remained.

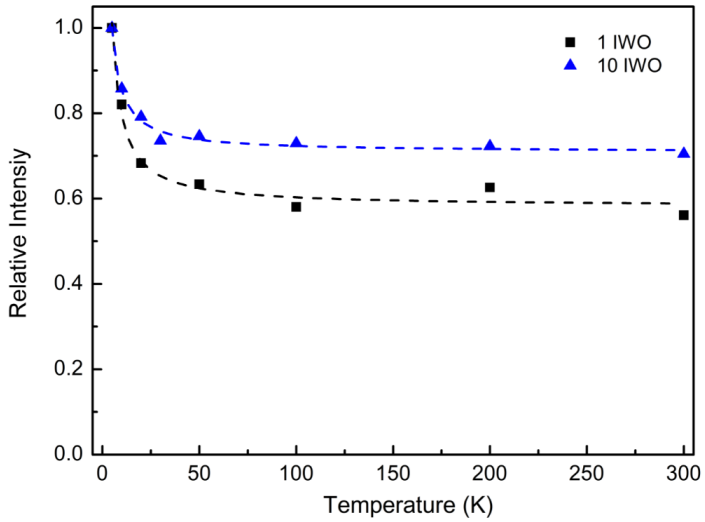

Figure 4.11: Temperature dependence of the MCD intensity for 1 % IWO NCs (black points) and 10 % IWO NCs (blue points). The dashed lines are the best fit to the experimental data using Curie's law. The maximum MCD absorption intensity at 5 K for both IWO NCs are normalized to 1.

The temperature dependence of the MCD intensity for 1 % IWO NCs and 10 % IWO NCs are shown in Figure 4.11, which are corresponding to the variable-temperature MCD spectra presented in Figure 4.9 (c) and Figure 4.10 (c), respectively. The MCD signals of both W-doped In_2O_3 NCs with low and high doping concentrations can be fitted to the Curie's law well which confirms the Curie-type paramagnetism. The fitting indicates the anomalous Zeeman

splitting of the ground state in IWO NCs induced by the paramagnetism due to the W^{5+} ions in the nanocrystals which come from the reduction of W^{6+}.[52] In addition, it can be observed that about 15 % more MCD intensity remains at room temperature when the doping concentration of tungsten increases as a result of the stronger LSPR strength induced to the nanocrystals.

In conclusion, significant difference of the magnetic field dependence and temperature dependence can be found between 1 % IWO NCs and 10 % IWO NCs due to the different LSPR strength of these doped nanocrystals. Stronger LSPR of 10 % IWO NCs which results in a stronger plasmon-exciton coupling is considered to be responsible for the linear dependence of the external magnetic field. The temperature field dependence which fits to Curie's law perfectly might cause by the various amount of reduced W^{6+} in the nanocrystals.

Chapter 5. Conclusions

Since molybdenum and tungsten are transition metal elements from the same group with comparable physical and chemical properties, their doping effects are expected to be similar. The results of this thesis demonstrate a successful synthesis of molybdenum-doped In_2O_3 NCs and tungsten-doped In_2O_3 NCs with various doping concentrations through the colloidal synthesis method. The bulk bcc-In_2O_3 crystal structure of both Mo and W doped In_2O_3 NCs was retained confirmed by the powder XRD measurements. TEM images of both IMO and IWO NCs with different doping concentrations show that they have a comparable bipyramid shape and the forming of this shape might related to the growth of certain planes. In addition, the size of IMO and IWO NCs increases with the increasing doping concentrations without any aggregation.

The EDX analysis confirmed the existence of In and the doping elements which indicated that the dopants ions have been successfully incorporated into the host lattice. However, different incorporation efficiency can be found between Mo and W doping. At low doping level, the actual doping concentrations of both IMO and IWO NCs were close to the starting doping concentration while with the increasing doping concentration, the incorporation efficiency of IWO NCs is significantly lower than IMO NCs. This might be caused by the size difference between the dopant ions where Mo^{6+} (0.59 Å) is somewhat smaller than W^{6+} (0.60 Å)[77], so it is easier for Mo ions to incorporate into the host lattice. In addition, Mo and W dopants ions may occupy different coordination sites of the host lattice which can contribute to the reported observations. The comparison of actual doping concentration and LSPR energy of IMO and IWO NCs are summarized in Table 5.1.

The UV-Vis-NIR and FTIR measurements of IMO and IWO NCs have shown tunable LSPR in the MIR range through changing the doping concentrations. Interestingly, although the difference in the doping efficiency of IMO and IWO NCs can be found from the table, their adjustable plasmon resonance range is very similar, roughly from 0.22 eV to 0.34 eV. It is worth noting that for the 5 % IWO NCs which the actual doping concentration is 1.5 %, the LSPR energy is comparable to the 10 % IMO NCs with the actual doping concentration of 9.2 %. This phenomenon indicates that even though the IWO NCs have lower incorporation efficiency than IMO NCs, the W dopants still provide a large number of free electron carriers that generate the strong plasmon resonance at low doping concentration. Higher doping concentrations of IMO (Figure A1) and IWO NCs exhibit the decrease in band gap energy as well as LSPR energy which might imply that there is a doping limitation due the trap sites around the doping ions or the electrons scattering effects by the defects.[28]

Table 5.1: Comparison of actual doping concentration and LSPR energy of IMO and IWO NCs

IMO NCs	**Actual doping (%)**	**LSPR (eV)**	**IWO NCs**	**Actual doping (%)**	**LSPR (eV)**
1	0.3	0.22	**1**	0.4	0.24
5	4.2	0.31	**5**	1.5	0.32
10	9.2	0.34	**10**	6.1	0.30

In MCD measurements, similar trends can also be found between IMO and IWO NCs. With the increase in the doping concentrations as well as the LSPR absorption, the MCD intensity becomes dominated by negative signals which indicate the carrier polarization induced

by plasmon. Moreover, more MCD signals maintain with the increasing temperature which demonstrates the decreasing of the C-term MCD as the plasmon-exciton coupling increases with the stronger LSPR.

However, it is intriguing that there are some significant differences exist between these two doped In_2O_3 NCs. 1 % IMO and 1 % IWO NCs, which have similar actual doping concentrations and LSPR absorption, show completely different field dependence: 1 % IMO NCs show linear dependence of the external magnetic fields while the 1% IWO NCs fit the Brillouin function better. This might be associated with the doping ions with different oxidation states in the host lattice. One probable reason is that the amount of W^{5+} ions in IWO NCs is more than the amount of Mo^{5+} ions in IMO NCs, therefore, 1 % IWO NCs present the property of the Curie-type paramagnetism. In addition, from Figure 5.1 which presents the difference between their temperature dependences, it is obvious that more MCD intensity remains in the 1 % IMO NCs than 1 % IWO NCs at high temperature which can be another evidence of the hypothesis mentioned above that there is a large amount of W^{5+} in the 1 % IWO NCs.

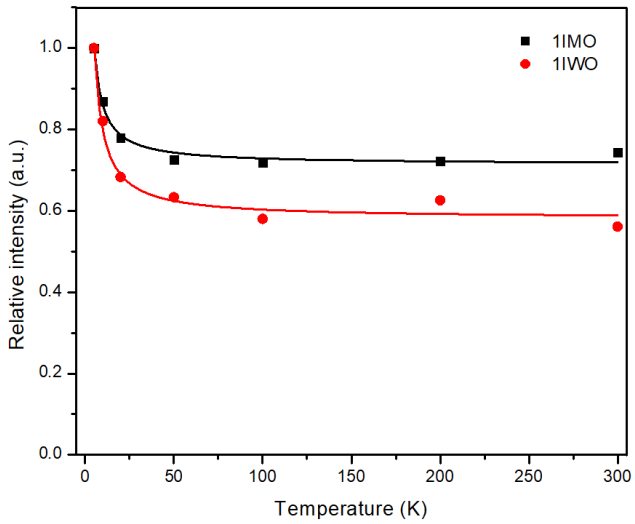

Figure 5.1: Temperature dependence of the MCD intensity for 1 % IMO NCs (black points) and 1 % IWO NCs (red points). The solid lines are the best fit to the experimental data using Curie's law. The maximum 5 K MCD absorption intensity is normalized to 1.

For 10 % IMO and 10 % IWO NCs, both MCD results show a linear relationship between the magnetic field and MCD intensity. The MCD intensity of 10 % IMO and 10 % IWO at 300 K, which can be considered as the temperature-independent A-term, is shown in Figure 5.2. The remaining MCD intensity in IWO NCs is as much as that in IMO NCs which might indicate that the ratio between the reduced doping ions and the original ones are similar or the effect of plasmon is similar due to their comparable LSPR oscillator strength.

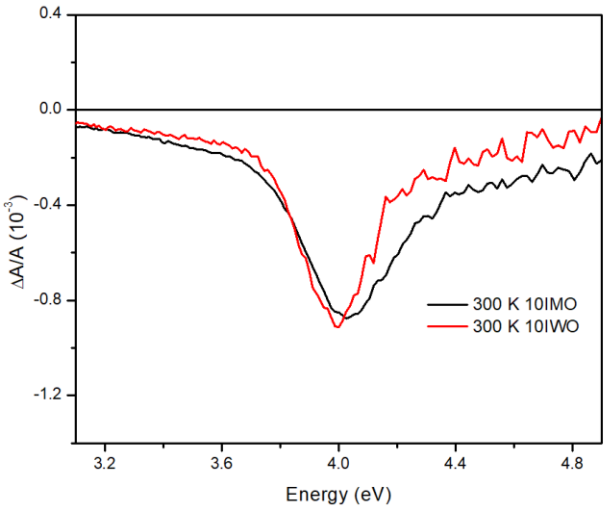

Figure 5.2: Normalized A-term MCD spectra of 10 % IMO (black trace) and 10 % IWO (red trace) collected at 300 K.

In conclusion, Mo and W doped In_2O_3 NCs were successfully synthesized for the first time and their plasmonic and magneto-optical properties were studied. Although these two similar transition metals are from the same group, differences in the doping effects can be found. For example, the incorporation efficiency and the different amount of oxidation states in the host lattice. The MCD measurements of these two doped NCs attest to the single-phase plasmon-exciton coupling and the temperature-persistent carrier polarization in plasmonic semiconductor nanocrystals.[52] The expansion of different types of doped NCs with these properties further helps explore the mechanism of the plasmon-induced carrier polarization and the applications of plasmonics.

In analogy to spintronics, which depends on the manipulation of the spin degree of freedom to realize charge carrier polarization, cyclotron magnetoplasmonic modes can also be applied in information processing and storage, which can be referred to as plasmontronics.[52] The excitation of the cyclotron magnetoplasmonic oscillations and Zeeman splitting of the band

states are caused by the non-resonant plasmon-exciton coupling, and this plasmon-exciton coupling also facilitates the dynamic control and manipulation of carrier polarization.[52] Using magnetoplasmonic modes as a new degree of freedom enables the light-induced carrier polarization in semiconductor nanocrystals, which can be achieved at room temperature due to the temperature independence of the magnetoplasmonic modes. These advantages also enable the possible technological applications of plasmonic semiconductor nanocrystals in photonics, quantum-information processing, and data storage.

Future Work

The plasmonic and magneto-optical properties of transition metal doped In_2O_3 NCs: IMO and IWO NCs have been studied, however, more experiments can be explored for further analysis. For both IMO and IWO NCs, the oxidation state of the doping ions especially the ratios of $[Mo^{5+}]/[Mo^{6+}]$ and $[W^{5+}]/[W^{6+}]$ are remaining as a challenging question because of the low signal-to-noise ratio in the XPS spectra. The X-ray absorption spectroscopy (XAS) measurement was performed for the IMO and IWO samples. More information could be obtained from the XAS data. For instance, the oxidation states of the doping ions and the occupation of indium coordination sites. However, it takes much time and effort to collect the information due to the professional knowledge required for analysing the XAS data.

Furthermore, a set of experiments that could be explored to determine the influence of different synthesis environment on the plasmonic and magneto-optical properties of IMO and IWO NCs. For instance, instead of running the synthesis under argon, an oxidizing environment such as air or a reducing environment such as hydrogen can be performed. The synthesis environment might affect vacancy defects and the shape of nanoparticles, and consequently, the LSPR and magnetoplasmonic properties. Therefore, it would be interesting to investigate the properties under various synthesis environment.

Finally, diverse types of precursors such as molybdenum (V) chloride ($MoCl_5$) and tungsten hexachloride (WCl_6) or different synthesis methods can be explored to study the impact on the doping efficiency and related properties and therefore, optimize the synthesis, quality, and properties of nanocrystals.

References

(1) Powell, D. H.; Helm, L.; Merbach, A. E. *Inorganic Chemistry*, Fifth edit.; Pearson: Toronto, 1991.

(2) Suresh, S. *Nanosci. Nanotechnol.* **2013**, *3*, 62–74.

(3) Jung, D.-R.; Kim, J.; Nahm, C.; Choi, H.; Nam, S.; Park, B. *Electron. Mater. Lett.* **2011**, *7*, 185–194.

(4) Robertson, J.; Gillen, R.; Clark, S. J. *Thin Solid Films* **2012**, *520*, 3714–3720.

(5) Van Hest, M. F. A. M.; Dabney, M. S.; Perkins, J. D.; Ginley, D. S. *Thin Solid Films* **2006**, *496*, 70–74.

(6) Warmsingh, C. *J. Appl. Phys.* **2004**, *95*, 3831.

(7) Coutts, T. J.; Young, D. L.; Li, X. *MRS Bull.* **2000**, *25*, 58–65.

(8) Hamberg, I.; Granqvist, C. G. *J. Appl. Phys.* **1986**, *60*, R123–R159.

(9) Murali, A.; Barve, A.; Leppert, V. J.; Risbud, S. H.; Kennedy, I. M.; Lee, H. W. H. *Nano Lett.* **2001**, *1*, 287–289.

(10) Farvid, S. S.; Dave, N.; Radovanovic, P. V. *Chem. Mater.* **2010**, *22*, 9–11.

(11) Xiao, Q.; Liu, Y.; Liu, L.; Li, R.; Luo, W.; Chen, X. *J. Phys. Chem. C* **2010**, *114*, 9314–9321.

(12) Farvid, S. S.; Dave, N.; Radovanovic, P. V. *Chem. Mater.* **2010**, *22*, 9–11.

(13) Ghodsi, V.; Layek, A.; Hegde, M.; Yildirim, B.; Radovanovic, P. V. *Chem. Commun.*

2016, *52*, 4353–4356.

(14) Farvid, S. S.; Radovanovic, P. V. *J. Am. Chem. Soc.* **2012**, *134*, 7015−7024.

(15) Shannon, R. D. *Solid State Commun.* **1966**, *4*, 629–630.

(16) Prewitt, C. T.; Shannon, R. D.; Rogers, D. B.; Sleight, A. W. *Inorg. Chem.* **1969**, *8*, 1985–1993.

(17) Epifani, M.; Siciliano, P.; Gurlo, A.; Barsan, N.; Weimar, U. *J. Am. Chem. Soc.* **2004**, *126*, 4078–4079.

(18) Yu, D.; Wang, D.; Qian, Y. *J. Solid State Chem.* **2004**, *177*, 1230–1234.

(19) Hutfluss, L. N.; Radovanovic, P. V. *J. Am. Chem. Soc.* **2015**, *137*, 1101–1108.

(20) Wang, T.; Radovanovic, P. V. *J. Phys. Chem. C* **2011**, *115*, 406–413.

(21) Farvid, S. S.; Dave, N.; Wang, T.; Radovanovic, P. V. *J. Phys. Chem. C* **2009**, *113*, 15928–15933.

(22) Mchale, J. M.; Auroux, A.; Perrotta, A. J.; Navrotsky, A. *Science* **1997**, *277*, 788–792.

(23) Zhang, H.; Banfield, J. F. *J. Mater. Chem.* **1998**, *8*, 2073–2076.

(24) Norris, D. J.; Efros, A. L.; Erwin, S. C. *Science* **2008**, *319*, 1776–1779.

(25) Turnbull, D. *J. Appl. Phys.* **1950**, *21*, 1022–1028.

(26) Dalpian, G. M.; Chelikowsky, J. R. *Phys. Rev. Lett.* **2006**, *96*, 1–4.

(27) Erwin, S. C.; Zu, L.; Haftel, M. I.; Efros, A. L.; Kennedy, T. A.; Norris, D. J. *Nature* **2005**, *436*, 91–94.

(28) Fang, H.; Hegde, M.; Yin, P.; Radovanovic, P. V. *Chem. Mater.* **2017**, *29*, 4970–4979.

(29) Dave, N.; Pautler, B. G.; Farvid, S. S.; Radovanovic, P. V. *Nanotechnology* **2010**, *21*.

(30) Farvid, S. S.; Ju, L.; Worden, M.; Radovanovic, P. V. *J. Phys. Chem. C* **2008**, *112*, 17755–17759.

(31) Maier, S. A.; Brongersma, M. L.; Kik, P. G.; Meltzer, S.; Requicha, A. A. G.; Atwater, H. A. *Adv. Mater.* **2001**, *13*, 1501–1505.

(32) El-Sayed, I. H.; Huang, X.; El-Sayed, M. A. *Nano Lett.* **2005**, *5*, 829–834.

(33) Novo, C.; Funston, A. M.; Mulvaney, P. *Nat. Nanotechnol.* **2008**, *3*, 598–602.

(34) Huang, X.; Jain, P. K.; El-Sayed, I. H.; El-Sayed, M. A. *Lasers Med. Sci.* **2008**, *23*, 217–228.

(35) Zeng, S.; Baillargeat, D.; Ho, H. P.; Yong, K. T. *Chem. Soc. Rev.* **2014**, *43*, 3426.

(36) Kanehara, M.; Koike, H.; Yoshinaga, T.; Teranishi, T. *Jacs Commun.* **2009**, *131*, 17736–17737.

(37) Mayer, K. M.; Hafner, J. H.; Antigen, A. À. *Chem. Rev.* **2011**, *111*, 3828–3857.

(38) Kreibig, U.; Vollmer, M. *Optical Properties of Metal Clusters*; 1995.

(39) Vestergaard, M. C.; Kerman, K.; Hsing, I. M.; Tamiya, E. *Nanobiosensors and Nanobioanalyses* **2015**, 1–379.

(40) Faucheaux, J. a.; Stanton, A. L. D.; Jain, P. K. *J. Phys. Chem. Lett.* **2014**, *5*, 976–985.

(41) Nütz, T.; Zum Felde, U.; Haase, M. *J. Chem. Phys.* **1999**, *110*, 12142–12150.

(42) Boltasseva, A.; Atwater, H. a. *Science* **2011**, *331*, 290–291.

(43) Buonsanti, R.; Llordes, A.; Aloni, S.; Helms, B. A.; Milliron, D. J. *Nano Lett.* **2011**, *11*, 4706–4710.

(44) Gordon, T. R.; Paik, T.; Klein, D. R.; Naik, G. V; Caglayan, H.; Boltasseva, A.; Murray, C. B. *Nano Lett.* **2013**, *13*, 2857–2863.

(45) Sachet, E.; Shelton, C. T.; Harris, J. S.; Gaddy, B. E.; Irving, D. L.; Curtarolo, S.; Donovan, B. F.; Hopkins, P. E.; Sharma, P. A.; Sharma, A. L.; et al. *Nat. Mater.* **2015**, *14*, 414–420.

(46) Mocatta, D.; Cohen, G.; Schattner, J.; Millo, O.; Rabani, E.; Banin, U. *Science* **2011**, *332*, 77–81.

(47) Abram, R. A.; Rees, G. J.; Wilson, B. L. H. *Adv. Phys.* **1978**, *27*, 799–892.

(48) Jin, S.; Lu, W.; Stanish, P. C.; Radovanovic, P. V. *Chem. Phys. Lett.* **2018**, *706*, 509–514.

(49) Lee, J.; Hernandez, P.; Lee, J.; Govorov, A. O.; Kotov, N. A. *Nat. Mater.* **2007**, *6*, 291–295.

(50) Uchida, K.; Adachi, H.; Kikuchi, D.; Ito, S.; Qiu, Z.; Maekawa, S.; Saitoh, E. *Nat. Commun.* **2015**, *6*, 1–8.

(51) Okamoto, K.; Niki, I.; Shvartser, A.; Narukawa, Y.; Mukai, T.; Scherer, A. *Nat. Mater.* **2004**, *3*, 601–605.

(52) Yin, P.; Tan, Y.; Fang, H.; Hegde, M.; Radovanovic, P. V. *Nat. Nanotechnol.* **2018**, 1–5.

(53) Okamoto, K.; Funato, M.; Kawakami, Y.; Tamada, K. *J. Photochem. Photobiol. C Photochem. Rev.* **2017**, *32*, 58–77.

(54) Zhang, J.; Tang, Y.; Lee, K.; Ouyang, M. *Nature* **2010**, *466*, 91–95.

(55) Fabian, J.; Sarma, S. Das. **2004**, *76*.

(56) Wolf, S. A.; Awschalom, D. D.; Buhrman, R. A.; Daughton, J. M.; Molna, S. Von. *Science* **2001**, *294*, 1488–1496.

(57) Hegde, M.; Farvid, S. S.; Hosein, I. D.; Radovanovic, P. V. *ACS Nano* **2011**, *5*, 6365–6373.

(58) Melander, E.; Östman, E.; Keller, J.; Schmidt, J.; Papaioannou, E. T.; Kapaklis, V.; Arnalds, U. B.; Caballero, B.; García-Martín, A.; Cuevas, J. C.; et al. *Appl. Phys. Lett.* **2012**, *101*, 063107.

(59) Uchida, H.; Masuda, Y.; Fujikawa, R.; Baryshev, A. V.; Inoue, M. *J. Magn. Magn. Mater.* **2009**, *321*, 843–845.

(60) Belotelov, V. I.; Akimov, I. A.; Pohl, M.; Kotov, V. A.; Kasture, S.; Vengurlekar, A. S.; Gopal, A. V.; Yakovlev, D. R.; Zvezdin, A. K.; Bayer, M. *Nat. Nanotechnol.* **2011**, *6*, 370–376.

(61) Mattei, G.; Caneschi, A.; Gatteschi, D.; Sangregorio, C. *Nano Lett.* **2013**, *13*, 4785–4789.

(62) Schimpf, A. M.; Lounis, S. D.; Runnerstrom, E. L.; Milliron, D. J.; Gamelin, D. R. *J. Am. Chem. Soc.* **2015**, *137*, 518–524.

(63) Schimpf, A. M.; Thakkar, N.; Gunthardt, C. E.; Masiello, D. J.; Gamelin, D. R. *ACS Nano* **2013**, *8*, 1065–1072.

(64) Ju, L.; Sabergharesou, T.; Stamplecoskie, K. G.; Hegde, M.; Wang, T.; Combe, N. A.;

Wu, H.; Radovanovic, P. V. *J. Am. Chem. Soc.* **2012**, *134*, 1136–1146.

(65) Farvid, S. S.; Sabergharesou, T.; Hutfluss, L. N.; Hegde, M.; Prouzet, E.; Radovanovic, P. V. *J. Am. Chem. Soc.* **2014**, *136*, 7669–7679.

(66) Wang, C. Y.; Dai, Y.; Pezoldt, J.; Lu, B.; Kups, T.; Cimalla, V.; Ambacher, O. *Cryst. Growth Des.* **2008**, *8*, 1257–1260.

(67) Cao, S.; Lee, J. Y.; Zhang, T.; Fisher, A. *J. Mater. Chem. C* **2018**, *6*, 4007–4014.

(68) Agrawal, A.; Cho, S. H.; Zandi, O.; Ghosh, S.; Johns, R. W.; Milliron, D. J. *Chem. Rev.* **2018**, *118*, 3121–3207.

(69) Zhang, Y.; Li, J.; Li, Q.; Zhu, L.; Liu, X.; Zhong, X.; Meng, J.; Cao, X. *Scr. Mater.* **2007**, *56*, 409–412.

(70) Yin, P.; Hegde, M.; Tan, Y.; Chen, S.; Garnet, N.; Radovanovic, P. V. *ACS Nano* **2018**, *12*, 11211–11218.

(71) Pineider, F.; Campo, G.; Bonanni, V.; Fernandez, C. D. J.; Mattei, G.; Caneschi, A.; Gatteschi, D.; Sangregorio, C. *Nano Lett.* **2013**, *13*, 4785–4789.

(72) Ding, D.; Huang, W.; Song, C.; Yan, M.; Guo, C.; Liu, S. *Chem. Commun.* **2017**, *53*, 6744–6747.

(73) Radović, M. et al. *J. Phys. D. Appl. Phys.* **2015**, *48*, 065301.

(74) Fedorov, A. V; Baranov, A. V; Inoue, K. *Phys. Rev. B* **1997**, *56*, 7491–7502.

(75) T. Itoh, M. Nishijima, A. I. Ekimov, C. Gourdon, Al. L. Efros, M. R. *Phys. Rev. Lett.* **1995**, *74*, 1645–1648.

(76) Beye, M.; Hennies, F.; Deppe, M.; Suljoti, E.; Nagasono, M.; Wurth, W.; Fo, A. *Phys. Rev. Lett.* **2009**, *103*, 237401.

(77) Shannon, B. Y. R. D.; H, M.; Baur, N. H.; Gibbs, O. H.; Eu, M.; Cu, V. *Acta Crystallogr. Sect. A* **1976**, *32*, 751–766.

Appendix

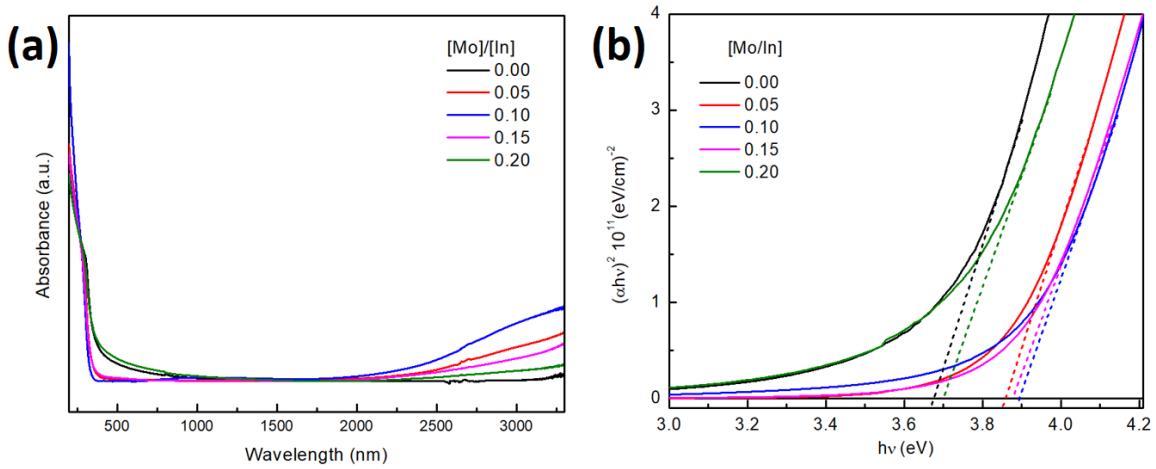

Figure A 1: (a) Band gap normalized UV-Vis-NIR absorption spectra of IMO NCs with different starting doping concentrations ([Mo]/[In]) indicated in the graph. (b) Tauc plot of IMO NCs with different doping concentrations showing red-shift of the optical band gap when the doping concentrations exceed 10 %.

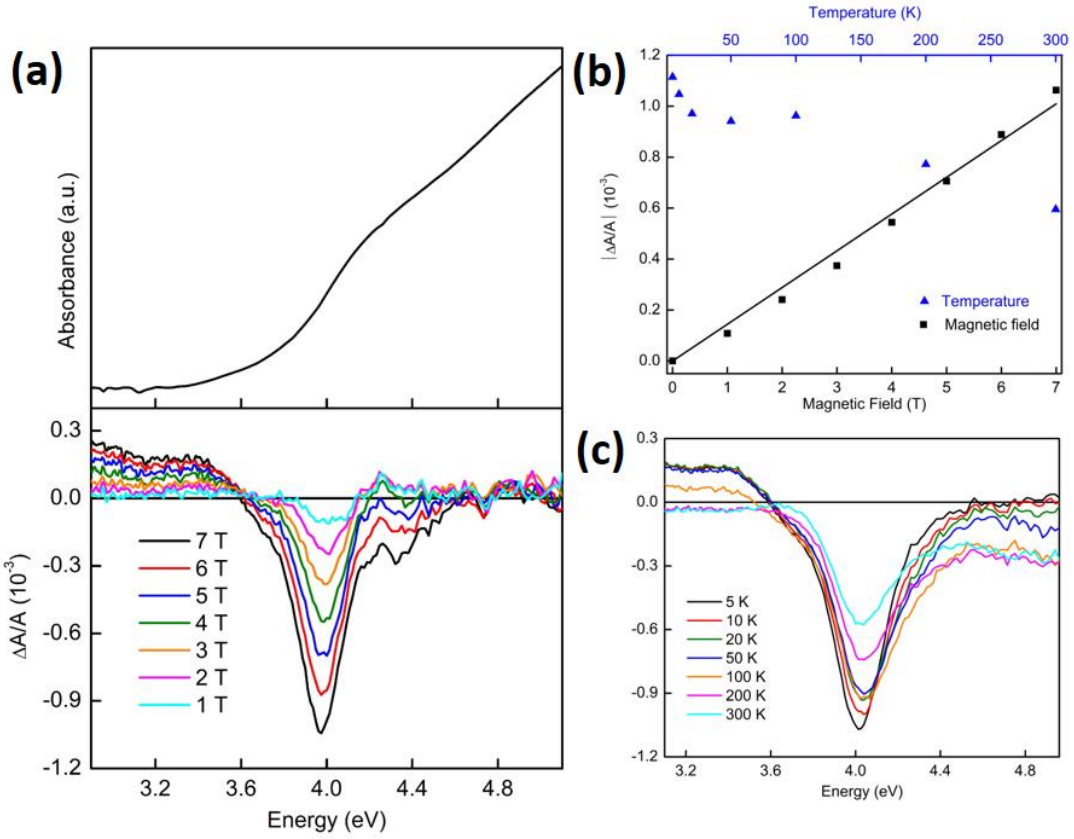

Figure A 2: : (a) Absorption (top) and MCD (bottom) spectra of IWO NCs with starting doping concentration [Mo]/[In]=0.03 collected at 5 K. MCD spectra collected at different external magnetic field strengths are indicated in the graph. (b) Magnetic field (black data points) dependence of MCD intensity recorded at 3.97 eV in (a). The black solid line is the linear fit to the data points. (c) The MCD spectra at 7 T in (a) are collected at different temperatures from 5 K to 300 K.

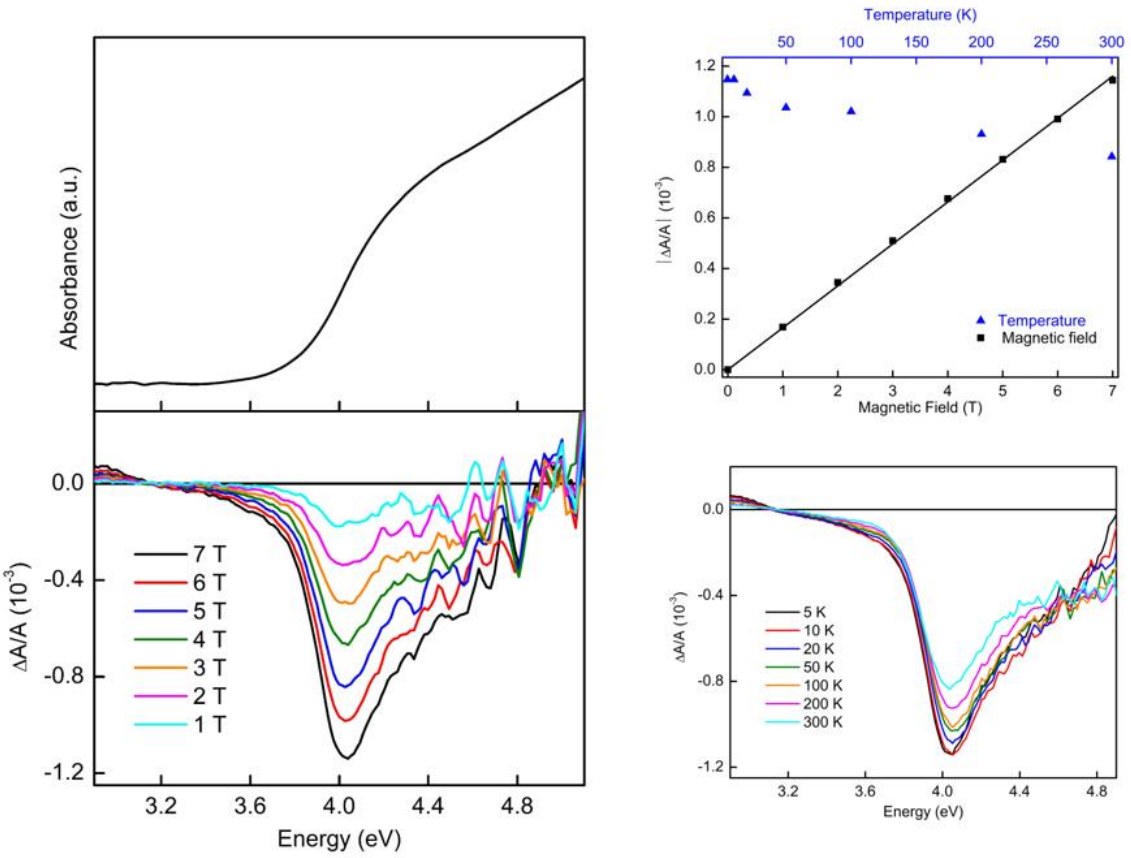

Figure A 3: (a) Absorption (top) and MCD (bottom) spectra of IWO NCs with starting doping concentration [Mo]/[In]=0.05 collected at 5 K. MCD spectra collected at different external magnetic field strengths are indicated in the graph. (b) Magnetic field (black data points) dependence of MCD intensity recorded at 4.02 eV in (a). The black solid line is the linear fit to the data points. (c) The MCD spectra at 7 T in (a) are collected at different temperatures from 5 K to 300 K.

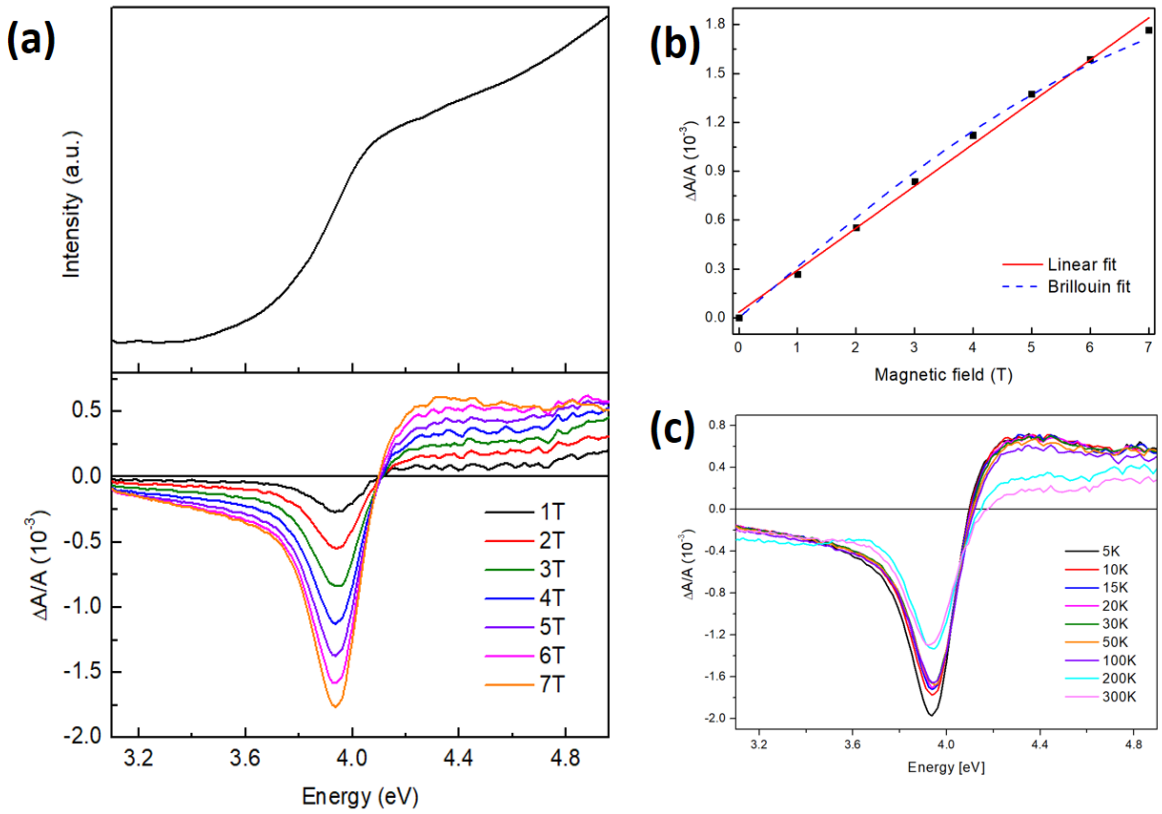

Figure A 4: (a) Absorption (top) and MCD (bottom) spectra of IWO NCs with starting doping concentration [W]/[In]=0.03 collected at 5 K. MCD spectra collected at different external magnetic field strengths are indicated in the graph. (b) Magnetic field (black data points) dependence of MCD intensity recorded at 3.93 eV for IWO NCs in (a). The red solid line and blue dashed line are the linear and Brillouin function fit to the data points, respectively. (c) The MCD spectra at 7 T of IWO NCs in (a) are collected at different temperatures (5 K - 300 K).